nature structural & molecular biology

Article

https://doi.org/10.1038/s41594-026-01830-7

PLA2G2F suppresses ferroptosis through phospholipid remodeling

Received: 23 September 2025

Accepted: 29 May 2026

Published online: 22 July 2026

Check for updates

Yingying Hu[1,2], Joleen Csuka[3], Presha Rajbhandari[4], Penghsuan Huang[5], Nicholas Carbone[1,2], Deguang Liang[1,6,7], Wei Gu[8,9], Alban Ordureau[1], Brent R. Stockwell[3,4,8,10] & Xuejun Jiang[1,2]

Ferroptosis is an iron-dependent form of regulated cell death driven by phospholipid peroxidation, and it has emerged as a potential therapeutic vulnerability of cancer. Here we identify the secretory phospholipase PLA2G2F (phospholipase A_2 group IIF) as a ferroptosis suppressor in bladder cancer and elucidate its regulation and mechanism of action. PLA2G2F functions through an intracellular mechanism by localizing to the endoplasmic reticulum to inhibit ferroptosis. Our genetic and pharmacological analyses reveal that peroxisome proliferator-activated receptor γ (PPARG), a nuclear hormone receptor and transcription factor previously implicated in ferroptosis regulation, upregulates PLA2G2F and that PPARG-mediated ferroptosis resistance is largely dependent on PLA2G2F in bladder cancer. Further, lipidomic profiling suggests that PLA2G2F preferentially acts on ether-linked phospholipids containing polyunsaturated fatty acids, thereby reducing the pool of peroxidation-prone polyunsaturated fatty acid-containing phospholipids. Together, our findings establish PLA2G2F as an endoplasmic reticulum-resident ferroptosis suppressor regulated by PPARG and show that inhibiting PPARG signaling or PLA2G2F activity can sensitize bladder cancer cells to ferroptosis induction.

Ferroptosis is a type of regulated cell death triggered by imbalances in iron, lipid metabolism and redox homeostasis[1,2]. It is involved in diverse pathological conditions, including cancer, degenerative diseases and ischemia/reperfusion. Given that ferroptosis arises from the accumulation of phospholipid peroxides—a product of metabolic activity—ferroptosis has been extensively investigated in metabolically active cancer cells. In the cell, three chemically distinctive mechanisms can prevent ferroptosis: one is mediated by glutathione peroxidase 4 (GPX4), which oxidizes glutathione from its reduced form (GSH) into its oxidized form (GSSG) while reducing phospholipid peroxides[3]; the second mechanism involves enzymes such as FSP1, DHODH and GCH1 that generate metabolites with radical-trapping antioxidant activity, which terminate phospholipid peroxidation and thus inhibit ferroptosis[4]; lastly, ferroptosis can also be kept in check by limiting the availability of the substrates for phospholipid peroxidation, that is, polyunsaturated fatty acid (PUFA)-containing phospholipids[5,6].

Cellular phospholipids can be classified based on the degree of acyl-chain saturation, ranging from saturated and monounsaturated to polyunsaturated. Monounsaturated fatty acid (MUFA)-containing phospholipids have been shown to protect against ferroptosis[7], while

[1]Cell Biology Program, Memorial Sloan Kettering Cancer Center, New York, NY, USA. [2]Tri-Institutional PhD Program in Chemical Biology, Memorial Sloan Kettering Cancer Center, New York, NY, USA. [3]Department of Chemistry, Columbia University, New York, NY, USA. [4]Department of Biological Sciences, Columbia University, New York, NY, USA. [5]Department of Chemistry, University of Wisconsin-Madison, Madison, WI, USA. [6]School of Basic Medical Sciences, Capital Medical University, Beijing, China. [7]Institute for Cancer Research, Chinese Institutes for Medical Research (CIMR), Beijing, China. [8]Herbert Irving Comprehensive Cancer Center, Columbia University, New York, NY, USA. [9]Institute for Cancer Genetics, Dept of Pathology and Cell Biology, Vagelos College of Physicians & Surgeons, Columbia University, New York, NY, USA. [10]Irving Institute for Cancer Dynamics, Data Science Institute, Columbia University Digestive and Liver Disease Research Center, Department of Pathology and Cell Biology, Columbia University, New York, NY, USA. e-mail: jiangx@mskcc.org

PUFA-containing phospholipids enhance ferroptosis susceptibility. As such, multiple enzymes regulate ferroptosis by altering the cellular phospholipid profile. For instance, acyl-CoA synthetase long-chain family member 3 (ACSL3) is known to activate MUFAs for incorporation into phospholipids and thereby suppresses ferroptosis[7], whereas acyl-CoA synthetase long-chain family member 4 (ACSL4) favors PUFA incorporation and promotes ferroptosis initiation[8]. Members of the membrane-bound *O*-acyl transferase (MBOAT) family, which remodel phospholipids, also participate in the modulation of ferroptosis sensitivity depending on their preference for activating different acyl chains for phospholipid synthesis[9]. Ether lipids have been shown to promote ferroptosis susceptibility[10], and more recently, di-PUFA-phosphatidylcholines (PCs) have been demonstrated to have a key role in driving ferroptosis[11,12], highlighting the importance of lipid acyl-chain composition in this specific form of cell death.

PLA2G2F (encoding phospholipase A_2 group IIF) was identified as a potential antiferroptosis gene in a genome-wide CRISPRa screen we conducted previously[5]. PLA2G2F belongs to group II of the PLA2 enzymes, categorized as the secretory PLA2 (sPLA2), as it characteristically contains an N-terminal signal peptide[13,14]. Following protein synthesis, the signal peptide of sPLA2 proteins is typically cleaved, targeting the protein into the secretory pathway, from which it can subsequently localize to specific cellular organelles, embed in membranes or be secreted extracellularly[15]. Although PLA2G2F is categorized as a secretory protein, the precise subcellular localization of PLA2G2F has not been defined experimentally.

PLA2G2F is highly expressed in skin and bladder tissues and is notably upregulated in bladder cancers (see later in the Results section). Its disease relevance and physiological roles have been more extensively studied in the skin, where *Pla2g2f*-knockout mice exhibited fragile stratum corneum, perturbed acidification and abnormal keratinocyte differentiation and gene expression[16,17]. However, the relevance of PLA2G2F in bladder cancer remains unexplored. Recently, several PLA2 family members have been implicated in ferroptosis regulation through their effects on labile lipid pools. For example, iPLA2β (PLA2G6), a Ca^{2+}-independent PLA2, hydrolyzes 15-HpETE-phosphatidylethanolamine (PE) and was shown to suppress p53-driven ferroptosis following reactive oxygen species (ROS)-induced stress[18,19]. Additionally, cytosolic PLA2 (cPLA2; PLA2G4A) suppresses ferroptosis by regulating arachidonic acid metabolism[20]. Another member, lipoprotein-associated PLA2 (Lp-PLA2; PLA2G7), was shown to remodel cellular PE and oleic acid, thus mitigating ferroptosis sensitivity[21]. However, despite these findings, the precise mechanisms by which PLA2 enzymes modulate ferroptosis remain incompletely understood, and their tissue-specific expression suggests differential regulation.

In this study, we show that PLA2G2F inhibits ferroptosis induced by both cysteine deprivation and GPX4 inhibition. Although PLA2G2F is classified as an sPLA2, we found that its intracellular activity is responsible for its ferroptosis-suppressing function. Immunofluorescence and co-immunoprecipitation mass spectrometry (IP–MS) revealed that PLA2G2F resides in the endoplasmic reticulum. Furthermore, we identify peroxisome proliferator-activated receptor γ (PPARG), a nuclear hormone receptor and transcriptional regulator previously implicated in ferroptosis regulation[22–28], as a key transcriptional regulator of *PLA2G2F*. We show that PLA2G2F regulates a phospholipid remodeling program that decreases the abundance of PUFA-containing phospholipids, particularly ether-linked PEs, leading to a cellular phospholipid state more resistant to ferroptosis.

Results

PLA2G2F inhibits ferroptosis

PLA2G2F contains a signal peptide on its N terminus (isoform 1; Fig. 1a and Extended Data Fig. 1a,b). Interestingly, the PLA2G2F protein might also be translated by using an alternative start codon upstream of and in frame with isoform 1, thus including an additional N-terminal extension and masking the signal peptide (isoform 2). To confirm the effect of PLA2G2F on ferroptosis inhibition, we generated three overexpression constructs harboring the open reading frames for isoform 1, isoform 2 and isoform 1 lacking the signal sequence (ΔN) (Fig. 1a). The ΔN construct was designed to assess the role of the signal peptide in protein expression and function. HT1080 and RT112 cell lines overexpressing C-terminally Flag-tagged PLA2G2F were generated and validated by western blot and reverse transcription followed by qPCR (RT–qPCR) (Fig. 1b,c). Interestingly, protein expression was not detectable from the ΔN construct, despite its mRNA expression levels being comparable to those of the other two constructs. Furthermore, isoform 1 and isoform 2 showed similar molecular weight, although the isoform 2 mRNA is supposed to encode an additional N-terminal extension (all these unusual properties of isoform 1, isoform 2 and ΔN were further analyzed in this study).

Next, we sought to confirm the ferroptosis-inhibitory activity of PLA2G2F. HT1080 cells overexpressing PLA2G2F were treated with the ferroptosis inducers (FINs) RSL3 (a class II FIN targeting GPX4)[29] or imidazole ketone erastin (IKE; a class I FIN inhibiting system x_c^-)[30] or underwent cystine starvation (Fig. 1d–f). As expected, ΔN PLA2G2F did not affect ferroptosis sensitivity in HT1080 cells, consistent with the lack of detectable protein expression. Overexpression of both isoform 1 and isoform 2 showed inhibitory effects toward ferroptosis induced by different triggers.

PLA2G2F exhibits tissue-specific expression in humans and is highly enriched in skin and bladder tissues[31–33]. Notably, our analysis of the cBioPortal database of patients with cancer[34–36] indicates that *PLA2G2F* is frequently overexpressed in bladder cancer (Extended Data Fig. 1c). Therefore, we selected the RT112 bladder cancer cell line with a high level of PLA2G2F expression to investigate its function in an endogenous context. *PLA2G2F* knockout was generated in RT112 cells using CRISPR–Cas9 with two single-guide RNAs (sgRNAs) targeting exon 2 of the *PLA2G2F* gene (Extended Data Fig. 1d; as a reliable anti-PLA2G2F antibody is not available, the two-sgRNA approach enabled the validation of knockout by genomic PCR), and PLA2G2F isoform 2 was reintroduced into the knockout cells (Extended Data Fig. 1e). *PLA2G2F* knockout in RT112 cells sensitized them toward ferroptosis induced by RSL3 and cystine starvation, both of which were rescued by re-expression of isoform 2 (Fig. 1g). The sensitization was also evidenced in both cell viability (Extended Data Fig. 1f) and lipid ROS intensity (Extended Data Fig. 1g). Notably, RT112 cells were intrinsically resistant toward IKE, and *PLA2G2F* knockout caused no significant change in sensitivity to IKE (Extended Data Fig. 1h). Consistent with HT1080 cells, overexpression of isoform 1 or isoform 2, but not ΔN, suppressed ferroptosis in RT112 cells (Fig. 1h,i and Extended Data Fig. 1i,j).

To further examine the role of the signal peptide in PLA2G2F expression, we generated two constructs with mutations in the signal peptide: PLA2G2F(ΔL53–V57) (SP_Δ), which has a shorter ER transmembrane H region of the peptide and is predicted to fail ER targeting, and PLA2G2F(A61Y/G63Y) (SP_YY), which harbors substitutions of two residues at the predicted cleavage site of the signal peptide[37]. Interestingly, both constructs resulted in a complete loss of protein signal by western blot despite a high mRNA expression level and a lack of the ability to inhibit ferroptosis (Extended Data Fig. 1k–m). Therefore, a functional signal peptide is essential for PLA2G2F. We also tested the 253J cell line, which is a bladder cancer cell line with low PLA2G2F expression, and showed that the overexpression of PLA2G2F had the same protective effect toward RSL3-induced ferroptosis in these cells (Extended Data Fig. 1n–o).

To examine whether the ferroptosis-inhibitory effect of PLA2G2F requires its enzymatic activity, we introduced an active site substitution, H110Q, in isoform 2 (ref. 38) (Extended Data Fig. 1p,q). Loss of activity in the H110Q mutant was confirmed with an in vitro enzymatic assay by incubating the immunoprecipitated mutant with

https://doi.org/10.1038/s41594-026-01830-7

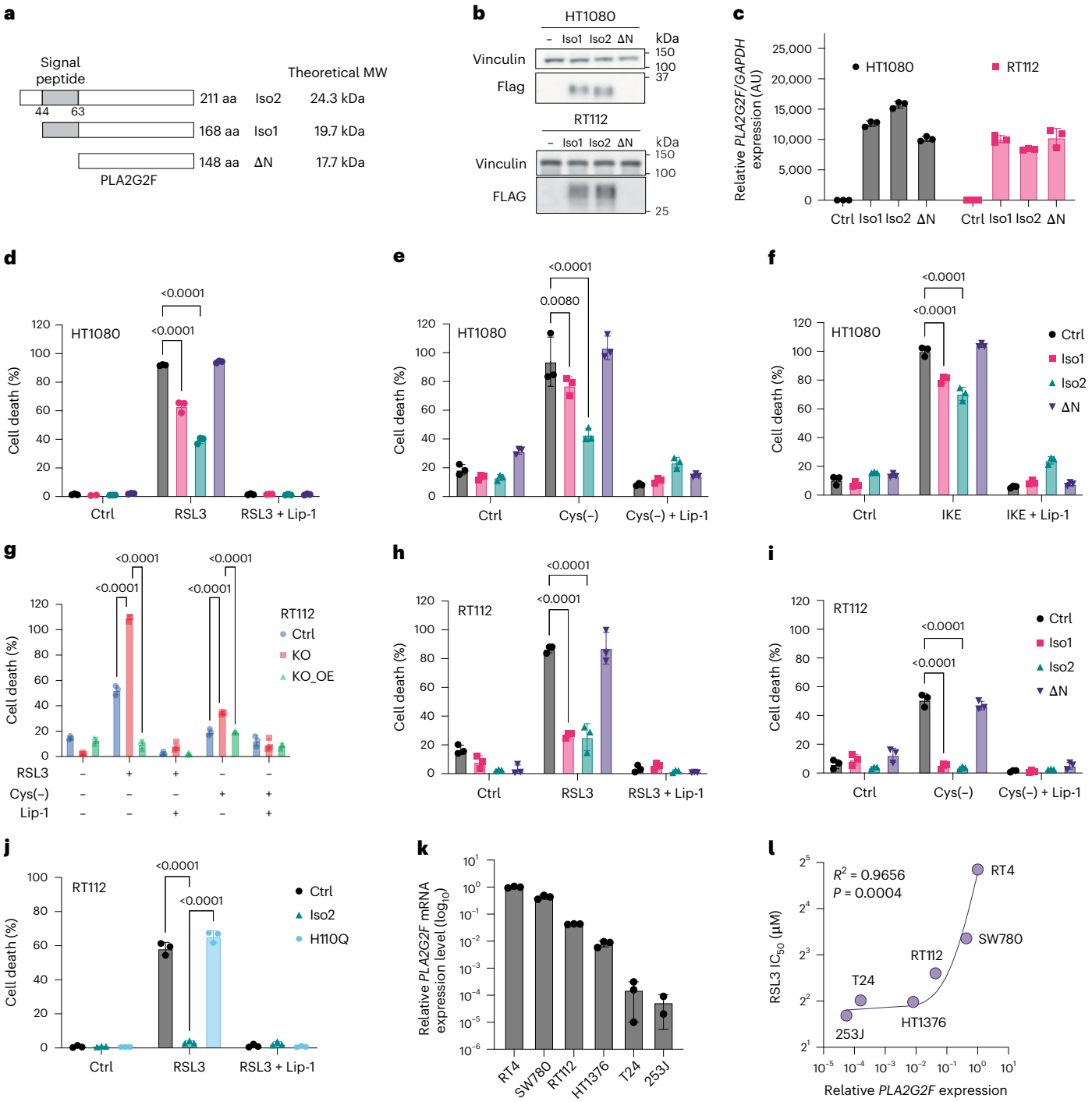

Fig. 1 | PLA2G2F inhibits ferroptosis. a, Design of PLA2G2F constructs to assess the activity of different isoforms. MW, molecular weight. **b**,**c**, Confirmation of PLA2G2F construct overexpression in HT1080 and RT112 cells using western blot (**b**) or RT–qPCR (**c**). AU, arbitrary units. **d**–**f**, Cell death of PLA2G2F-overexpressing HT1080 cells induced by 25 nM RSL3 at 16 hr (**d**), cystine starvation at 14 hr (**e**) or 0.5 μM IKE at 16 hr (**f**). **g**, Cell death of *PLA2G2F* knockout in RT112 cells with ferroptosis induced by 12.5 nM RSL3 and cystine starvation at 10 hr. KO, knockout; OE, overexpression. **h**,**i**, Cell death of PLA2G2F-expressing RT112 cells with ferroptosis induced by 12.5 nM RSL3 at 16 hr (**h**) or cystine starvation at 16 hr (**i**). **j**, Cell death in RT112 cells with PLA2G2F (H110Q) overexpression, with ferroptosis induced by 12.5 nM RSL3 for 10 hr. **k**, *PLA2G2F* expression level in a bladder cancer cell line panel. **l**, *PLA2G2F* expression versus RSL3 IC_{50} at 24 hr in the bladder cancer cell line panel. Liproxstatin 1 (Lip-1), 5 μM. Data are presented as mean ± s.d., $n = 3$ biologically independent samples (**c**–**l**). Statistical analysis was performed using two-way analysis of variance (ANOVA) (**d**–**j**) or two-tailed Pearson correlation analysis (**l**).

phospholipids, subsequently measuring the abundance of hydrolyzed products and remaining substrate (Extended Data Fig. 1r). As expected, overexpression of the H110Q mutant failed to cause resistance toward RSL3-induced ferroptosis (Fig. 1j), confirming that the ferroptosis-inhibitory effect of PLA2G2F is indeed executed through its enzymatic activity.

To evaluate the relationship between PLA2G2F expression and ferroptosis resistance, we analyzed a panel of bladder cancer cell lines. Ferroptosis sensitivity was assessed by measuring RSL3 half-maximal inhibitory concentration (IC_{50}) values using the CellTiter-Glo assay for cell viability (Extended Data Fig. 1s). *PLA2G2F* mRNA levels, quantified via RT–qPCR (Fig. 1k), showed a positive linear correlation with RSL3

https://doi.org/10.1038/s41594-026-01830-7

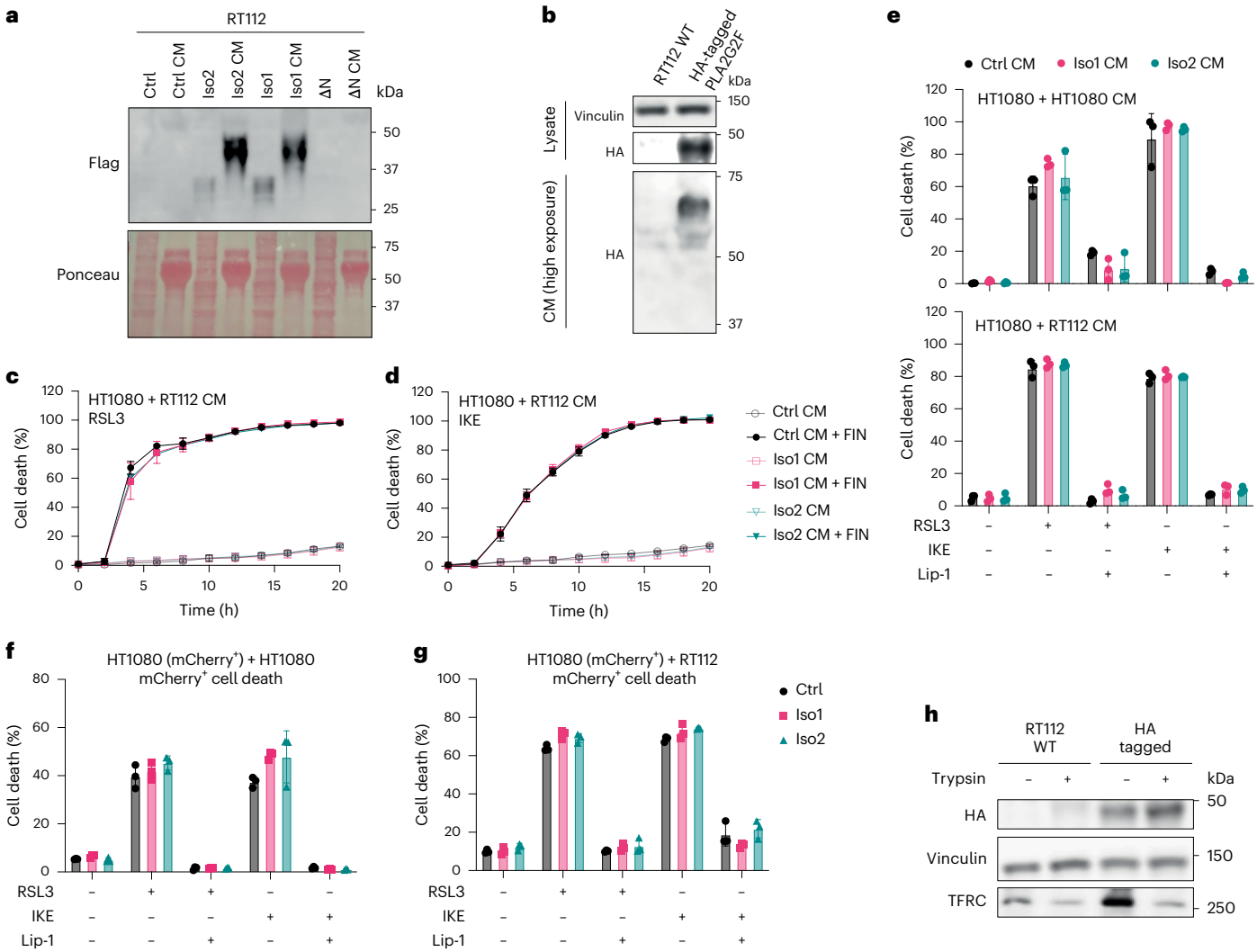

Fig. 2 | PLA2G2F inhibits ferroptosis through intracellular mechanisms. **a**, Western blot of conditioned medium (CM) from PLA2G2F-overexpressing RT112 cells. **b**, Western blot of conditioned medium from RT112 cells with endogenous HA-tagged PLA2G2F. WT, wild type. **c**,**d**, Cell death curves of wild-type (WT) HT1080 cells cultured in conditioned medium from PLA2G2F-overexpressing RT112 cells. Cells were treated with 25 nM RSL3 (**c**) or 0.5 μM IKE (**d**). **e**, Cell death of wild-type HT1080 cells cultured for 10 hr in conditioned medium from PLA2G2F-overexpressing HT1080 (top) or RT112 (bottom) cells. **f**,**g**, Cell death of H2B-mCherry-labeled HT1080 cells co-cultured with PLA2G2F-overexpressing HT1080 cells (**f**) or RT112 cells (**g**) at 12 hr. Cells were treated with 25 nM RSL3, 0.5 μM IKE and/or 5 μM Lip-1 as indicated. **h**, Western blot of RT112 cells with endogenous HA-tagged PLA2G2F pretreated with trypsinization. Lip-1, 5 μM. Data are presented as mean ± s.d., $n = 3$ biologically independent samples (**c**–**g**).

IC_{50} values (Fig. 1l), indicating that a higher level of PLA2G2F expression is associated with stronger resistance to ferroptosis. These results support the notion that PLA2G2F suppresses ferroptosis in bladder cancer.

PLA2G2F inhibits ferroptosis through intracellular mechanisms

Previous studies have primarily focused on isoform 1 (ref. 13) or a protein sequence lacking the signal peptide[16,17] and shown that, when incubated with cultured cells, the recombinant protein lacking the signal peptide could penetrate and disrupt lipid monolayers and bilayers or enter the cell[38]. These findings raise the possibility that PLA2G2F may inhibit ferroptosis through an extracellular mechanism.

To test this possibility, we started by collecting and concentrating conditioned medium from cells overexpressing each construct and performed western blot analysis. Interestingly, for both isoforms 1 and 2, we observed a Flag-tagged protein of higher-molecular weight in the conditioned medium in comparison with the proteins in the cell lysates (Fig. 2a and Extended Data Fig. 2a). A similar higher-molecular-weight product was also detected in conditioned medium derived from cells expressing endogenous HA-tagged PLA2G2F (Fig. 2b). To determine whether this shift in molecular weight reflects glycosylation associated with PLA2G2F secretion, we treated both cell lysates and conditioned medium samples with PNGase F to remove N-linked glycans. Surprisingly, PNGase F treatment reduced the molecular weight of both fractions, but the extracellular signal still showed a higher molecular weight, suggesting that both intracellular and secreted PLA2G2F are glycosylated and that the secreted form possesses additional modification(s) not susceptible to PNGase F activity (Extended Data Fig. 2b).

We next sought to investigate whether secreted PLA2G2F contributes to ferroptosis suppression. We cultured wild-type HT1080 cells in concentrated conditioned medium derived from PLA2G2F-overexpressing cell lines (Fig. 2c–e and Extended Data Fig. 2c,d) or in that derived from RT112 control or *PLA2G2F*-knockout cells (Extended Data Fig. 2e,f) and subsequently measured ferroptosis induction. Ferroptosis sensitivity was not altered upon treatment with these different sources of conditioned medium. In addition, we also performed co-culture experiments. HT1080 cells with H2B-mCherry

(mCherry$^+$ fusion protein) were co-cultured with either HT1080 cells (Fig. 2f and Extended Data Fig. 2g) or RT112 cells (Fig. 2g and Extended Data Fig. 2h) expressing vector control or overexpressing PLA2G2F (mCherry$^-$) and then subjected the cultures to ferroptosis induction with RSL3. Compared with vector control, PLA2G2F overexpression inhibited ferroptosis in mCherry$^-$ cells (cell autonomous) but not in mCherry$^+$ cells (cell non-autonomous). Conversely, *PLA2G2F* knockout affected RT112 cells (mCherry$^-$, cell autonomous) but not the co-cultured HT1080 cells (mCherry$^+$, noncell autonomous) in ferroptosis sensitivity (Extended Data Fig. 2i,j). These findings further support the idea that PLA2G2F does not inhibit ferroptosis through an extracellular mechanism.

Is it possible that PLA2G2F is secreted but is tightly associated with the membrane of the cell in which it is synthesized? In such a model, extracellular PLA2G2F would only function in a cell-autonomous fashion. To test this, we trypsinized PLA2G2F-overexpressing cells before western blot analysis. If PLA2G2F were associated with the outer membrane, trypsin treatment would reduce its signal, as seen in the transferrin receptor control (Fig. 2h). However, the Flag signal remained unchanged, indicating that there was not a substantial amount of excreted PLA2G2F that was associated with the outer membrane of the cell. Taking these findings together, we conclude that PLA2G2F exerts its ferroptosis-inhibitory effect intracellularly.

PLA2G2F localizes in the ER with its signal peptide cleaved

Because the cDNAs of isoform 1 and isoform 2 produce proteins with similar molecular weights, we sought to analyze their respective protein products by MS analysis. Immunoprecipitation was performed, followed by MS (Fig. 3a, b). Three unique peptide sequences were quantified and analyzed, with two corresponding to the N-terminal extension of isoform 2 and one being shared by both isoforms. As anticipated, the peptides specific to isoform 2 were not detected or quantified in isoform 1-overexpressing cells. A strong signal of the shared peptide was observed in both cell types. Surprisingly, MS analysis detected low levels of peptides corresponding to the N-terminal extension of isoform 2 in isoform 2-overexpressing cells (Fig. 1b).

The results of the MS analysis raised the following question: Does the mRNA transcript for isoform 2 encode this additional N-terminal extension upstream of the sequence encoding the signal peptide? To investigate this, we designed two pairs of RT–qPCR primers, one for the coding sequence of the N-terminal extension and the other for the adjacent signal peptide sequence. RT–qPCR with the two primer sets produced comparable signals in isoform 2-overexpressing cells, confirming that the extension sequence is an integral part of the mRNA (Fig. 3c, d). We made the same observation in wild-type RT112 cells expressing endogenous PLA2G2F (Extended Data Fig. 3a), indicating that, at least in these cells, isoform 2 is the major mRNA transcript for *PLA2G2F*.

We further searched for peptide fragments corresponding to the signal peptide sequence in our IP–MS dataset (Extended Data Fig. 3b). The abundance of signal peptide-specific peptides was low compared with that of the common peptide located further downstream, suggesting that the signal sequence is cleaved from the mature, stable form of the PLA2G2F protein translated from both mRNA isoforms. This explains how isoform 1 and isoform 2 constructs produce proteins with the same molecular weight (Fig. 1b). For the N-terminal extension sequence in isoform 2, it is possible that either the start codon immediately upstream of the signal peptide is preferentially used for protein translation or the additional N-terminal sequence of isoform 2 is cleaved right after its translation.

Cleavage of the signal peptide from the mature PLA2G2F protein prompted us to determine its intracellular localization. We conducted immunofluorescence imaging of PLA2G2F coupled with markers for different cellular organelles (Fig. 3e,f). PLA2G2F from both isoform constructs showed the strongest colocalization with the ER marker PDI, indicating ER localization. Consistent with this conclusion, MS analysis of PLA2G2F co-immunoprecipitation products revealed that its interacting proteins are predominantly enriched for ER proteins (Extended Data Fig. 3c), which was also supported by a Gene Ontology (cellular component) analysis (Extended Data Fig. 3d). Based on the observations from IP–MS and confocal imaging, we propose that the signal peptide of PLA2G2F guides its translocation into the ER where the signal peptide is proteolytically removed.

To further test this hypothesis, we expressed a fusion protein linking the PLA2G2F signal peptide to green fluorescent protein (GFP) in RT112 cells. We also expressed mCherry-tagged Sec61β in the cells as an ER membrane marker. With super-resolution microscopy, we saw a clear overlap of GFP with Sec61β, demonstrating that PLA2G2F signal peptide can direct GFP to the ER (Extended Data Fig. 3e).

PLA2G2F is a transcriptional target of PPARG and mediates the ferroptosis-inhibitory function of PPARG

Given that PLA2G2F is a lipid-modifying enzyme, we hypothesized that its expression may be regulated by lipid metabolism-related transcription factors. We performed a transcription factor prediction using the ALGGEN-PROMO tool[39] on the genomic sequence spanning 500 bp upstream and downstream of the *PLA2G2F* gene. The TRANSFAC v8.3 model identified 69 potential transcription factors with a dissimilarity margin of ≤15%. Among those candidates, we focused on lipid metabolism-related transcription factors. With this criterion, the PPAR and retinoid X receptor (RXR) families were identified. Notably, PPAR family members are known to bind to RXR family members to form a heterodimer transcription factor complex[40]. Further, expression data from the public database DepMap (https://depmap.org/portal/)[41] show a positive correlation between *PPARG* and *PLA2G2F* expression levels in bladder cancer (Extended Data Fig. 4a), and online chromatin immunoprecipitation and sequencing (ChIP–seq) databases[42] show various binding peaks of PPARG on the *PLA2G2F* gene (Extended Data Fig. 4b). To verify those *PLA2G2F* peaks, we conducted a ChIP–qPCR on the RT112 bladder cancer cell line, by designing five sets of primers, each targeting a peak that was identified from the online ChIP–seq databases (Extended Data Fig. 4b). The results showed that PPARG can bind to these five peaks, and importantly, binding of PPARG with peak 3 (P3; corresponding to chr1: 20152436–20152715) was upregulated upon treatment with PPARG agonist GW1929 (Fig. 4a).

To assess transcriptional regulation by the candidate transcription factors, RT112 cells were treated with various agonists for those transcription factors, and the PLA2G2F mRNA and protein levels were measured (Fig. 4b,c). Of all agonists tested, the PPARG agonists produced the most robust upregulation of PLA2G2F. PPARG agonist activity was further confirmed with the upregulation of *FABP4*, a PPARG target gene[43]. (Fig. 4c). This induction was consistently observed across a panel of bladder cancer cell lines (Fig. 4d). PPARG is a potential cancer therapeutic target[44], and it has also been implicated in ferroptosis inhibition with underlying mechanisms not well defined[22–28]. As several ferroptosis genes have been reported to be regulated by PPARG agonists[23,45–47], we also measured the impact of PPARG agonists on a series of ferroptosis-related genes. While PPARG agonists may regulate *MBOAT1* and *GPX4* rather modestly, if at all, the magnitude of induction was significantly lower than that of *PLA2G2F* and the known PPARG target *FABP4*(Extended Data Fig. 4c).

To determine whether PPARG suppresses ferroptosis specifically through PLA2G2F, we conducted cell death assays using the PPARG agonists GW1929 and rosiglitazone in control cells and *PLA2G2F*-knockout cells (Fig. 4e,f and Extended Data Fig. 4d). In control cells, RSL3-induced ferroptosis was significantly attenuated by PPARG agonist treatment. However, this protective effect was largely abolished in *PLA2G2F*-knockout cells. The overexpression of PLA2G2F in RT112 cells protected cells against RSL3 regardless of the state of PPARG signaling (Extended Data Fig. 4e,f), further supporting the idea

https://doi.org/10.1038/s41594-026-01830-7

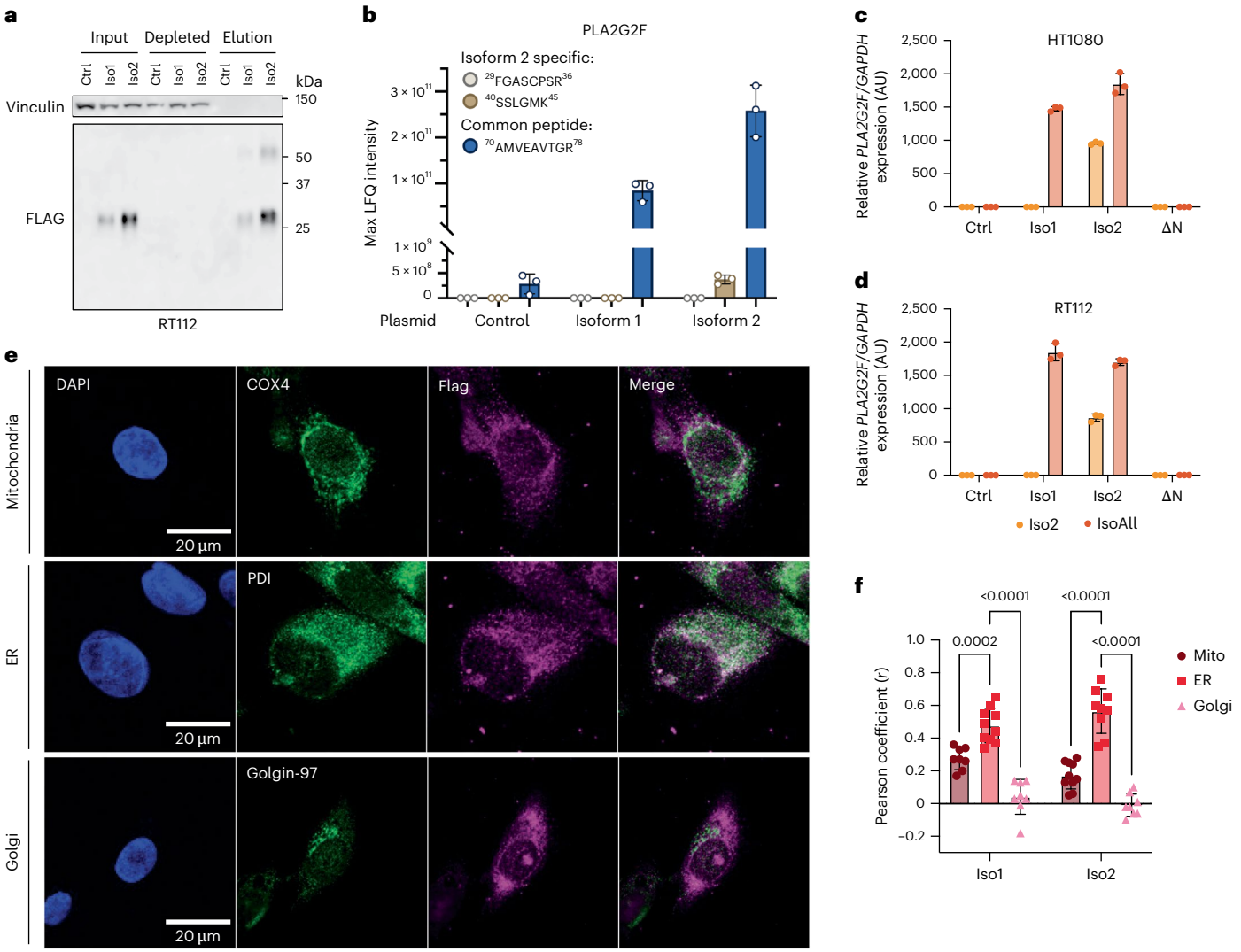

Fig. 3 | PLA2G2F inhibits ferroptosis in the ER. a, Western blot of anti-Flag immunoprecipitation in PLA2G2F-overexpressing RT112 cells. **b**, MS signal intensity of isoform 2-specific peptides and common peptide following anti-FLAG immunoprecipitation in PLA2G2F-overexpressing RT112 cells. LFQ, label-free quantification. **c**,**d**, RT–qPCR of isoform 2-specific or signal peptide-specific mRNA sequences in PLA2G2F-overexpressing HT1080 cells (**c**) or RT112 cells (**d**). **e**, Representative images of isoform 2 colocalization with different cellular organelle markers in RT112 cells from $n = 2$ independent experiments. **f**, Pearson coefficient of the fluorescence signals from immunofluorescence showing colocalization of PLA2G2F with the ER marker. Mito, mitochondria. Data are presented as mean ± s.d., $n = 3$ biologically independent samples (**b**–**d**) or mean ± s.d., $n = 8$ technical replicates for the mitochondria and Golgi groups, $n = 10$ technical replicates for the ER group (**f**). Statistical analysis was performed using two-way ANOVA (**f**).

that PLA2G2F is the primary functional effector in this context. Furthermore, we generated *PPARG*-knockdown RT112 cells (Fig. 4g) and found that both the induction of *PLA2G2F* and the ferroptosis-inhibitory effects of PPARG agonists were effectively neutralized (Fig. 4h,i and Extended Data Fig. 4g,h). These results demonstrate that PLA2G2F is crucial for PPARG-mediated ferroptosis suppression in these bladder cancer cells.

PLA2G2F promotes ferroptosis resistance through phospholipid remodeling

Our work indicates that the catalytic activity of the lipid metabolic enzyme PLA2G2F is required for its capability to suppress ferroptosis (Fig. 1j). To further investigate the underlying mechanism, we conducted an untargeted lipidomic analysis on RT112 cells overexpressing PLA2G2F (isoform 2) versus vector control, as well as *PLA2G2F*-knockout versus wild-type cells (Fig. 5a,b and Extended Data Fig. 5a). Significant alteration of cellular lipid species was induced by both overexpression and knockout of PLA2G2F.

In terms of free fatty acids, we observed that the abundance of free PUFAs increased in PLA2G2F-overexpressing cells and decreased in knockout cells (Fig. 5c and Extended Data Fig. 5b), likely due to the enzymatic cleavage activity of PLA2G2F. For lysophospholipids (LPLs), free PUFA levels were overall elevated in PLA2G2F-overexpressing cells and lowered in the knockout group, which was particularly the case for ether-linked LPLs (Fig. 5d,e). Combined, these findings suggest that PLA2G2F preferentially cleaves ether-linked phospholipids with PUFA chains at the sn-2 position, releasing free PUFAs and ether-linked LPLs. Note that, due to the isobaric nature of plasmanyl (O-) and plasmenyl (P-) species, ether-linked lipids are annotated based on MS-DIAL output[48,49]; however, these assignments remain structurally ambiguous at the MS1 and MS2 levels.

For PE species, the alteration appears to be more complicated (Extended Data Fig. 5c). Among those significantly altered PEs, we found that abundant PUFA-containing PE species, especially ether-linked PEs, were downregulated in the overexpressing group (Fig. 5e). Conversely, these species that were significantly upregulated

https://doi.org/10.1038/s41594-026-01830-7

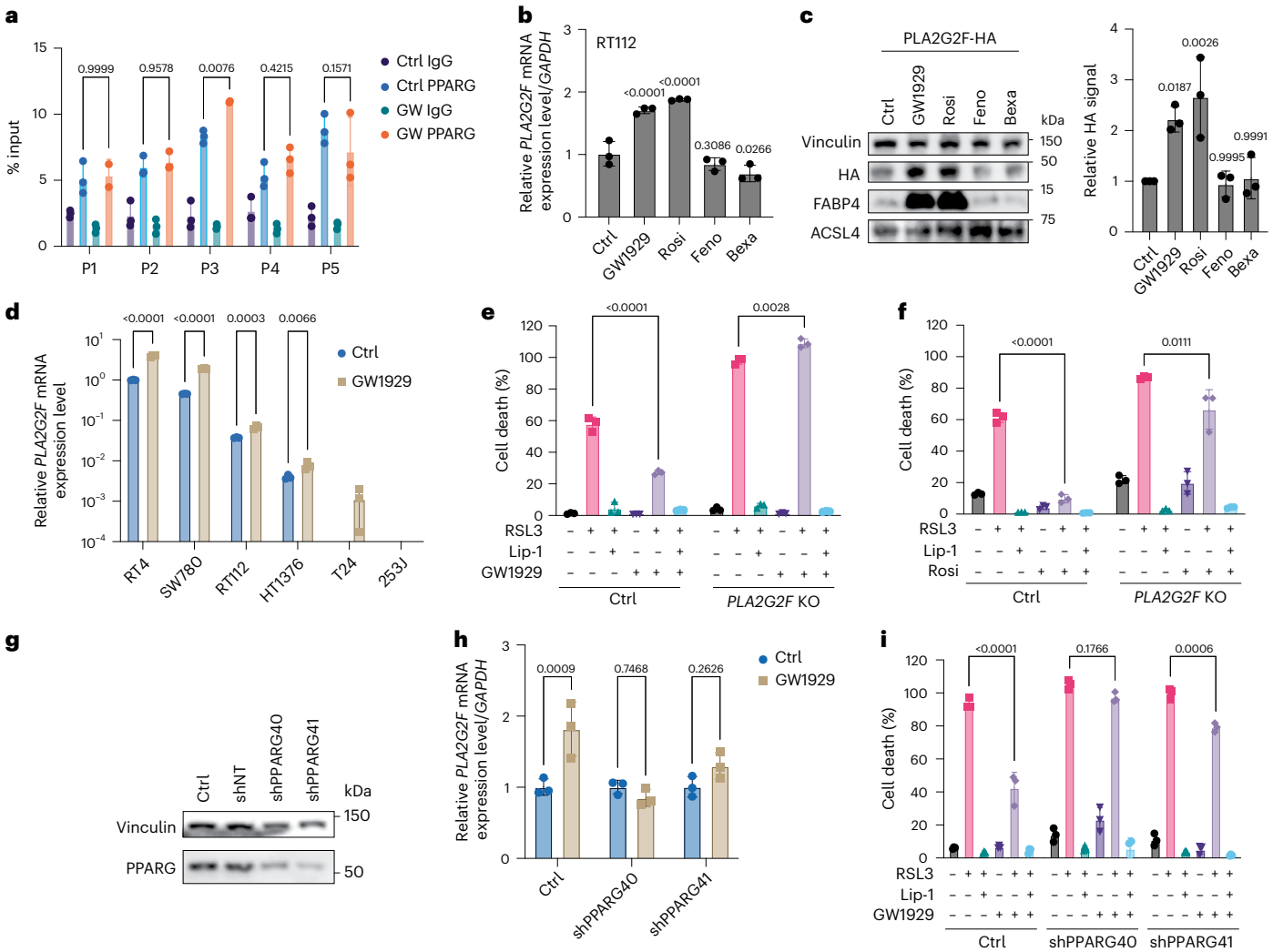

Fig. 4 | PPARG suppresses ferroptosis in a PLA2G2F-mediated manner in bladder cancer cells. a, ChIP–qPCR results showing binding and regulation of *PLA2G2F* by PPARG in RT112 cells. GW, GW1929; P, peak. **b**,**c**, RT–qPCR (**b**) and western blot (**c**, left) of PLA2G2F levels with various agonist treatments for 48 hr. The PLA2G2F–HA signal from the western blot was quantified, showing a ~2.5-fold increase under PPARG agonist treatment (**c**, right panel). GW1929, 10 μM; rosiglitazone (Rosi), 20 μM; fenofibrate (Feno), 25 μM; and bexarotene (Bexa), 1 μM. **d**, RT–qPCR of *PLA2G2F* levels with 10 μM GW1929 for 48 hr in the bladder cancer cell line panel. **e**,**f**, Cell death of *PLA2G2F*-knockout cells with 10 μM GW1929 (48-hr pretreatment) at 12 hr (**e**) or 20 μM rosiglitazone (48-hr pretreatment) at 14 hr (**f**). **g**, Western blot of PPARG knockdown in RT112 cells. **h**, RT–qPCR of *PPARG*-knockdown RT112 cells with 10 μM GW1929 (48-hr pretreatment) at 12 hr. **i**, Cell death of RT112 cells with *PPARG* knockdown with 10 μM GW1929 (48-hr pretreatment) at 14 hr. RSL3, 12.5 nM; Lip-1, 5 μM. Data are presented as mean ± s.d., $n = 3$ biologically independent samples (**a**–**f**,**h**,**i**). Statistical analysis was performed using two-way ANOVA (**a**–**c**,**e**,**f**,**i**) or unpaired two-tailed *t* test (**d**,**h**).

in the knockout group contained PUFA tails (Fig. 5b). To further examine the differences among distinct lipid classes, we calculated the normalized fold change in LPLs with different head groups that are diacyl or ether-linked lipids (Extended Data Fig. 5d). We saw a higher fold change in ether-linked lysophosphatidylethanolamines (LPEs) in comparison with the other lipid classes. Enrichment analysis further supported a preferential decrease in the abundance of ether-linked PUFA-containing phospholipids in PLA2G2F- overexpressing cells (Extended Data Fig. 5e). Notably, the proportion of significantly altered PUFA-containing phospholipids was higher than that of MUFA-containing phospholipids in both PLA2G2F-overexpressing and knockout cells (Extended Data Fig. 5f). We note that stoichiometrically the decrease in phospholipid abundance did not match perfectly with the increase in the abundance of corresponding LPLs. This is expected in untargeted lipidomics due to differential ionization efficiencies and dynamic ranges, as well as the relatively rapid metabolic turnover of LPLs in cellular remodeling pathways.

To further assess the substrate preference of PLA2G2F, we conducted in vitro enzymatic assays using affinity-purified proteins and equimolar combinations of phospholipid substrates in the form of liposomes. We directly compared preferences across three structural features: acyl-chain saturation (PUFA- versus MUFA-containing phospholipids), linkage type (diacyl versus ether-linked phospholipids) and head group (PE versus PC). Consistent with our cellular observations, PLA2G2F exhibited a stronger hydrolysis of PUFA-containing and ether-linked phospholipids compared with their MUFA-containing and diacyl-linked counterparts, respectively, and a more potent hydrolysis was also seen in PE over PC substrate (Fig. 5g,h). Together, these biochemical data demonstrate that PLA2G2F possesses a distinct kinetic preference for PUFA-containing ether-linked PEs.

In contrast with PUFA-containing PEs, PUFA-containing phosphatidylglycerol and phosphatidylinositol species had increased abundance in PLA2G2F-overexpressing cells (Extended Data Fig. 5g). Notably, the overall abundance of phosphatidylglycerol and

https://doi.org/10.1038/s41594-026-01830-7

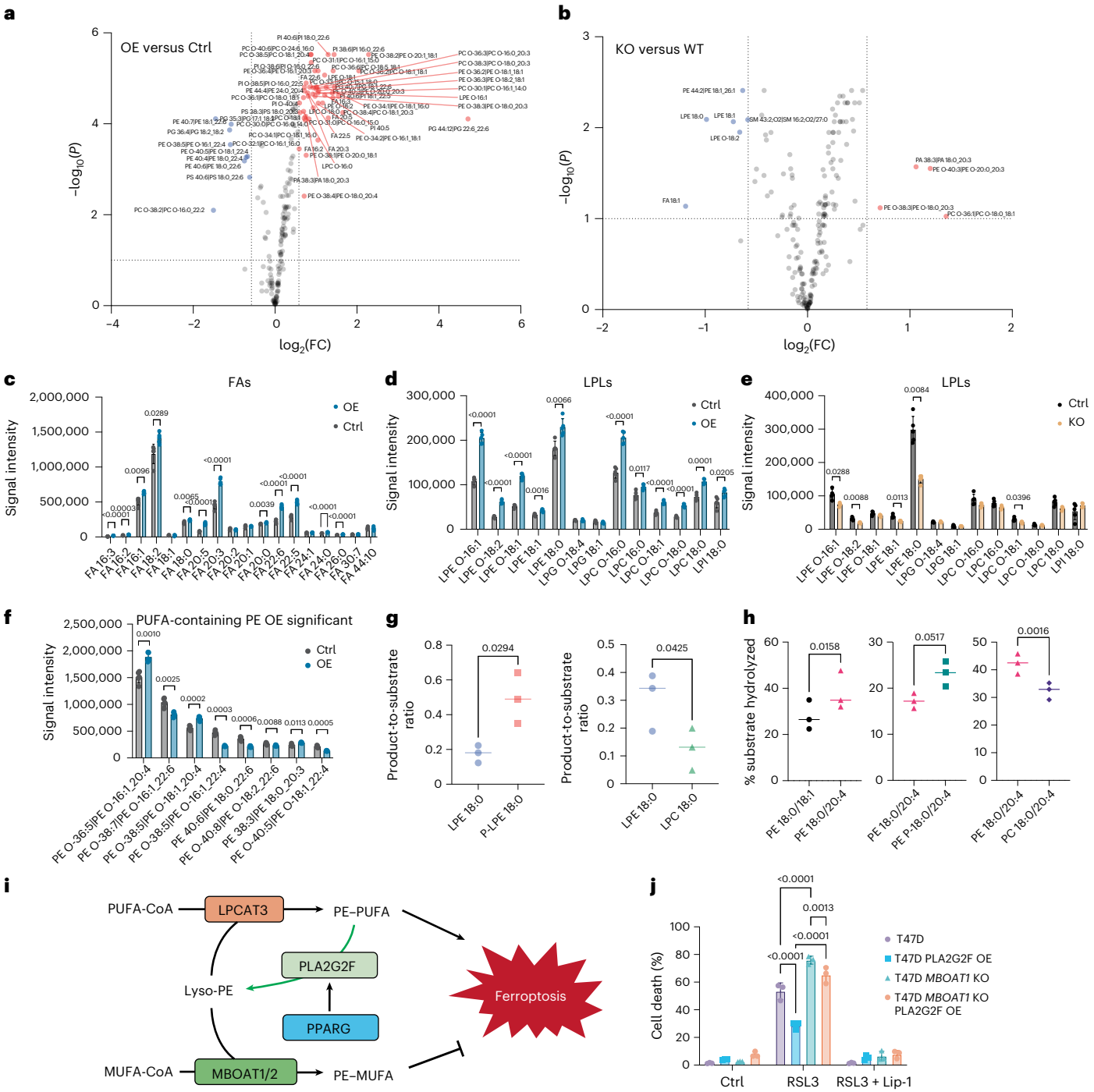

Fig. 5 | Lipidomic analysis of the effect of PLA2G2F on the cellular lipidome. **a**, Volcano plot from lipidomic analysis of PLA2G2F-overexpressing versus control RT112 cells. Red represents upregulated lipids and blue represents downregulated lipids in overexpression cells. FC, fold change. **b**, Volcano plot of lipidomic analysis from *PLA2G2F*-knockout versus wild-type RT112 cells. Red represents upregulated lipids and blue represents downregulated lipids in knockout cells. **c**,**d**, Lipidomic signal intensity of identified fatty acids (FAs) (**c**) and LPLs (**d**) in PLA2G2F-overexpressing versus control (ctrl) RT112 cells. **e**, Lipidomic signal intensity of identified LPLs in *PLA2G2F*-knockout versus wild-type RT112 cells. **f**, Lipidomic signal intensity of the most abundant PUFA-containing PEs identified in PLA2G2F-overexpressing versus control RT112 cells. **g**, Product-to-substrate ratio of LPE versus P-LPE (left) and LPE versus LPC (right) in an vitro enzymatic assay of PLA2G2F. **h**, Percentage of substrate hydrolyzed in the MUFA- versus PUFA-containing PE group (left), the diacyl- versus ether-linked PE group (middle) and the PE versus PC group (right) in an vitro enzymatic assay. **i**, Model showing how PLA2G2F promotes ferroptosis resistance. **j**, Cell death of *MBOAT1*-knockout T47D cells with or without PLA2G2F overexpression, upon treatment with 12.5 nM RSL3 for 24 hr. Lip-1, 5 µM. Data are presented as mean ± s.d., $n = 5$ biologically independent samples (**c**–**f**) or $n = 3$ biologically independent samples (**g**–**h**,**j**). Statistical analysis was performed using multiple *t* tests with adjusted *P* value (Bonferroni correction) (**a**,**b**), unpaired two-tailed *t* test (**c**–**h**) or two-way ANOVA (**j**). Note that, due to the isobaric nature of plasmanyl (O-) and plasmenyl (P-) species, ether-linked lipids are annotated based on MS-DIAL output; however, these assignments remain structurally ambiguous at the MS1 and MS2 levels.

phosphatidylinositol species was lower than that of PE species, suggesting a limited contribution to the total lipid pool compared with primary changes observed in the PE fraction.

Ether-linked phospholipids have been implicated in ferroptosis induction, although the underlying mechanisms remain unclear[10,50], and PUFA-containing PEs are well-established promoters of ferroptosis[8,9]. Therefore, our data support the following model wherein PLA2G2F reduces the cellular pool of PUFA-containing PEs, especially ether-linked PEs, thereby shifting the composition of the cellular lipidome from one with more oxidation-sensitive PUFA-containing PEs toward one with more MUFA-containing PEs, resulting in increased ferroptosis resistance (Fig. 5h).

To further clarify the relationship of such a change in phospholipid profile with ferroptosis resistance, we investigated the contribution of the phospholipid remodeling enzymes, MBOAT1/MBOAT2. T47D breast cancer cell line was used, which predominantly expresses ER-regulated MBOAT1 instead of MBOAT2 for its ferroptosis resistance[5]. We overexpressed PLA2G2F in both control and *MBOAT1*-knockout T47D cells and measured their sensitivity to ferroptosis (Fig. 5j and Extended Data Fig. 5h). As expected, we observed a strong ferroptosis inhibition effect upon PLA2G2F overexpression in wild-type T47D cells, but PLA2G2F overexpression led to a noticeable but much attenuated inhibitory effect on ferroptosis in *MBOAT1*-knockout cells (Fig. 5j), likely because the loss of MBOAT1 remodels the phospholipid profile toward high abundance of PUFA-containing phospholipids, rendering PLA2G2F overexpression on the *MBOAT1*-knockout background far less effective in suppressing ferroptosis.

Discussion

In this study, we demonstrate that a high level of PLA2G2F expression contributes to ferroptosis resistance in bladder cancer and that PPARG transcriptionally upregulates PLA2G2F. This finding has clinical implications because of the role of PPARG in determining bladder cancer subtype. Bladder cancer is broadly classified into luminal papillary (~80%) and basal nonpapillary (~20%) subtypes, which differ in pathology, prognosis and therapeutic response[51]. Luminal papillary tumors are typically less invasive but are generally less immune responsive and prone to recurrence. A hallmark of the luminal subtype is elevated PPARG expression[52], which drives urothelial differentiation and is genetically activated in ~20–25% of these tumors[52,53]. In this study, all PLA2G2F-high bladder cancer cell lines we used (RT112, SW780 and RT4) belong to the luminal papillary subtype with a high level of PPARG expression[54], consistent with our finding that PPARG transcriptionally upregulates PLA2G2F. Given that the luminal bladder cancer subtype displays reduced ferroptosis sensitivity[55,56], our data provide a mechanistic explanation for such subtype-specific resistance and suggest that disruption of the PPARG–PLA2G2F axis could sensitize luminal bladder cancers to ferroptosis-inducing therapies. Beyond cancer, PLA2G2F has also been implicated in aging and in maintaining lipid homeostasis in a mouse model of neurodegeneration[57]. Together, these observations suggest that PLA2G2F may have a broader role in cellular lipid regulation across distinct disease contexts, while the mechanistic basis and pathological consequences appear to be context dependent. Further, an interesting question for future research is whether the ferroptosis-suppressive role of PLA2G2F contributes to processes such as aging and neurodegeneration.

This study has revealed some intriguing cellular and molecular features of PLA2G2F. Although PLA2G2F is characterized as a secreted enzyme because of the presence of a putative signal peptide sequence, a substantial portion of the PLA2G2F protein remains inside the cell, at least for its ferroptosis-suppressing activity. Remarkably, the intracellular ER localization of the enzyme appears to require the signal peptide, and without it, the protein might not be properly synthesized or be rapidly degraded, as no stable protein was observed for the ΔN form (Fig. 1b). Is such degradation due to misfolding of the protein in the cytoplasm (that is, certain additional processes inside of the ER facilitate proper folding of PLA2G2F after the signal peptide is removed), or is the degradation triggered by its recognition by a specific cytoplasmic E3 ubiquitin ligase, although it can be folded correctly in the cytoplasm? The latter possibility suggests that accidental leakage of the enzyme to the cytoplasm might be unfavorable biologically and thus needs to be efficiently eliminated. If so, what is this unfavorable consequence? Further, a form of PLA2G2F that is potentially secreted and extracellular was observed, although it exhibited a higher-molecular weight but lacked ferroptosis-inhibitory activity (Fig. 2 and Extended Data Fig. 2). Is there any specific posttranslational modification that dictates whether PLA2G2F should remain in the ER or be secreted? What is the biological function of the secreted PLA2G2F? Does the presumed secretion-specific modification alter the enzymatic activity of PLA2G2F? Although not immediately relevant to ferroptosis, all these questions warrant further investigation.

Importantly, this study also suggests a certain level of substrate preference for PLA2G2F and, speculatively, for other members of the PLA2 family. Our lipidomic and biochemical analyses lend evidence toward the possibility that PLA2G2F preferentially cleaves the PUFA chain at the sn-2 position of ether-linked PE species. It will be important to determine the structural basis for PLA2G2F to favor ethanolamine as the head group or the ether link at the sn-1 position of its phospholipid substrate. Speculatively, the preference of PLA2G2F for ether-linked phospholipids may be further reinforced by subcellular compartmentation. The biosynthesis of ether-linked phospholipids is initiated in the peroxisome and completed in the ER before these phospholipids are transported to the plasma membrane[58]. Given that PLA2G2F is localized to the ER, its physical proximity to these species likely facilitates efficient substrate access. Furthermore, because PLA2G2F exhibits a preference for ether-linked substrates, the basal rate of biosynthesis of ether-linked lipids could dictate the total substrate availability for PLA2G2F-mediated remodeling.

Our lipidomic analysis also revealed that the decrease in PUFA-containing PEs caused by PLA2G2F was accompanied by a concurrent increase in PUFA-containing phosphatidylglycerol and phosphatidylinositol species. This observation suggests a potential metabolic redistribution, where free PUFAs released from PEs by PLA2G2F activity might be re-incorporated into other phospholipids. While definitive quantification of this flux would require future isotope-tracing studies and the biological relevance of the concurrent increase of phosphatidylglycerol and phosphatidylinositol species is not clear, the steady-state increase in phosphatidylglycerol/phosphatidylinositol species highlights the complexity of the lipid remodeling landscape induced by PLA2G2F.

Remarkably, in addition to PLA2G2F, several other PLA2 family members have also been shown to promote ferroptosis resistance[18–21]. Do they all recognize PUFAs at the sn2 position of phospholipids, or do they preferentially cleave damaged fatty acyl chains (PUFAs are susceptible to damage by oxidation) of phospholipids to surveil phospholipid integrity and homeostasis, as proposed previously[9,59]? In either case, the underlying mechanisms need to be defined. Furthermore, given the distinct expression, regulation and biological roles of various PLA2 family members[60], it will be interesting to investigate whether ferroptosis suppression contributes to their corresponding biological functions.

Lastly, this and previous studies appear to pinpoint to a shared, common paradigm in that various nuclear hormone receptors transcriptionally regulate the expression of specific lipid metabolic enzymes, which in turn alter the cell's sensitivity to ferroptosis induction. For example, in addition to the PPARG–PLA2G2F axis revealed in this study, estrogen receptor and androgen receptor regulate MBOAT1 and MBOAT2, respectively, with both leading to cellular phospholipid remodeling and enhanced resistance to ferroptosis[5]. Other recent studies have reported similar mechanisms for FXR, RXR and additional nuclear receptors, further supporting the generality of this

paradigm[61–65]. The effect of these various nuclear hormone receptors on ferroptosis might be 'coincidental' due to the central role of lipid metabolism in ferroptosis. On the other hand, and beyond ferroptosis, the biological logic of this common paradigm of the regulation of lipid metabolism by a variety of nuclear hormone signaling pathways warrants further in-depth investigation.

Online content

Any methods, additional references, Nature Portfolio reporting summaries, source data, extended data, supplementary information, acknowledgments, peer review information; details of author contributions and competing interests; and statements of data and code availability are available at https://doi.org/10.1038/s41594-026-01830-7.

References

1. Jiang, X., Stockwell, B. R. & Conrad, M. Ferroptosis: mechanisms, biology and role in disease. *Nat. Rev. Mol. Cell Biol.* **22**, 266–282 (2021).
2. Dixon, S. J. et al. Ferroptosis: an iron-dependent form of nonapoptotic cell death. *Cell* **149**, 1060–1072 (2012).
3. Yang, W. S. et al. Regulation of ferroptotic cancer cell death by GPX4. *Cell* **156**, 317–331 (2014).
4. Punziano, C., Trombetti, S., Cesaro, E., Grosso, M. & Faraonio, R. Antioxidant systems as modulators of ferroptosis: focus on transcription factors. *Antioxidants* **13**, 298 (2024).
5. Liang, D. et al. Ferroptosis surveillance independent of GPX4 and differentially regulated by sex hormones. *Cell* **186**, 2748–2764.e22 (2023).
6. Liang, D., Minikes, A. M. & Jiang, X. Ferroptosis at the intersection of lipid metabolism and cellular signaling. *Mol. Cell* **82**, 2215–2227 (2022).
7. Magtanong, L. et al. Exogenous monounsaturated fatty acids promote a ferroptosis-resistant cell state. *Cell Chem. Biol.* **26**, 420–432.e9 (2019).
8. Doll, S. et al. ACSL4 dictates ferroptosis sensitivity by shaping cellular lipid composition. *Nat. Chem. Biol.* **13**, 91–98 (2017).
9. Kim, J. W., Lee, J. Y., Oh, M. & Lee, E. W. An integrated view of lipid metabolism in ferroptosis revisited via lipidomic analysis. *Exp. Mol. Med.* **55**, 1620–1631 (2023).
10. Zou, Y. et al. Plasticity of ether lipids promotes ferroptosis susceptibility and evasion. *Nature* **585**, 603–608 (2020).
11. Qiu, B. et al. Phospholipids with two polyunsaturated fatty acyl tails promote ferroptosis. *Cell* **187**, 1177–1190.e18 (2024).
12. Samovich, S. N. et al. Strikingly high activity of 15-lipoxygenase towards di-polyunsaturated arachidonoyl/adrenoyl-phosphatidylethanolamines generates peroxidation signals of ferroptotic cell death. *Angew. Chem. Int. Ed. Engl.* **63**, e202314710 (2024).
13. Valentin, E. et al. Cloning and recombinant expression of human group IIF-secreted phospholipase A_2. *Biochem. Biophys. Res. Commun.* **279**, 223–228 (2000).
14. Teufel, F. et al. SignalP 6.0 predicts all five types of signal peptides using protein language models. *Nat. Biotechnol.* **40**, 1023–1025 (2022).
15. Owji, H., Nezafat, N., Negahdaripour, M., Hajiebrahimi, A. & Ghasemi, Y. A comprehensive review of signal peptides: structure, roles, and applications. *Eur. J. Cell Biol.* **97**, 422–441 (2018).
16. Murakami, M., Yamamoto, K. & Taketomi, Y. Phospholipase A_2 in skin biology: new insights from gene-manipulated mice and lipidomics. *Inflamm. Regen.* **38**, 31 (2018).
17. Yamamoto, K. et al. The role of group IIF-secreted phospholipase A_2 in epidermal homeostasis and hyperplasia. *J. Exp. Med.* **212**, 1901–1919 (2015).
18. Chen, D. et al. iPLA2β-mediated lipid detoxification controls p53-driven ferroptosis independent of GPX4. *Nat. Commun.* **12**, 3644 (2021).
19. Sun, W. Y. et al. Phospholipase iPLA2β averts ferroptosis by eliminating a redox lipid death signal. *Nat. Chem. Biol.* **17**, 465–476 (2021).
20. Zhao, R. et al. ATF6α promotes prostate cancer progression by enhancing PLA2G4A-mediated arachidonic acid metabolism and protecting tumor cells against ferroptosis. *Prostate* **82**, 617–629 (2022).
21. Oh, M. et al. The lipoprotein-associated phospholipase A_2 inhibitor darapladib sensitises cancer cells to ferroptosis by remodelling lipid metabolism. *Nat. Commun.* **14**, 5728 (2023).
22. Han, L. et al. PPARG-mediated ferroptosis in dendritic cells limits antitumor immunity. *Biochem. Biophys. Res. Commun.* **576**, 33–39 (2021).
23. Duan, C. et al. Activation of the PPARγ prevents ferroptosis-induced neuronal loss in response to intracerebral hemorrhage through synergistic actions with the Nrf2. *Front Pharmacol.* **13**, 869300 (2022).
24. Xue, X. et al. PPARγ activation suppresses chondrocyte ferroptosis through mitophagy in osteoarthritis. *J. Orthop. Surg. Res.* **18**, 620 (2023).
25. Yakubov, E. et al. Ferroptosis and PPAR-γ in the limelight of brain tumors and edema. *Front Oncol.* **13**, 1176038 (2023).
26. Pan, H. et al. A nutrient-deficient microenvironment facilitates ferroptosis resistance via the FAM60A–PPAR axis in pancreatic ductal adenocarcinoma. *Research* **7**, 0300 (2024).
27. Lai, W., Yu, L. & Deng, Y. PPARγ alleviates preeclampsia development by regulating lipid metabolism and ferroptosis. *Commun. Biol.* **7**, 429 (2024).
28. Zhang, S. et al. PPARγ antagonists exhibit antitumor effects by regulating ferroptosis and disulfidptosis. *Biomolecules* **14**, 596 (2024).
29. Yang, W. S. & Stockwell, B. R. Synthetic lethal screening identifies compounds activating iron-dependent, nonapoptotic cell death in oncogenic-RAS-harboring cancer cells. *Chem. Biol.* **15**, 234–245 (2008).
30. Dolma, S., Lessnick, S. L., Hahn, W. C. & Stockwell, B. R. Identification of genotype-selective antitumor agents using synthetic lethal chemical screening in engineered human tumor cells. *Cancer Cell* **3**, 285–296 (2003).
31. Weinstein, J. N. et al. The Cancer Genome Atlas Pan-Cancer analysis project. *Nat. Genet.* **45**, 1113–1120 (2013).
32. Lonsdale, J. et al. The Genotype-Tissue Expression (GTEx) project. *Nat. Genet.* **45**, 580–585 (2013).
33. Tang, Z., Kang, B., Li, C., Chen, T. & Zhang, Z. GEPIA2: an enhanced web server for large-scale expression profiling and interactive analysis. *Nucleic Acids Res.* **47**, W556–W560 (2019).
34. Cerami, E. et al. The cBio Cancer Genomics Portal: an open platform for exploring multidimensional cancer genomics data. *Cancer Discov.* **2**, 401–404 (2012).
35. Gao, J. et al. Integrative analysis of complex cancer genomics and clinical profiles using the cBioPortal. *Sci. Signal.* **6**, pl1 (2013).
36. de Bruijn, I. et al. Analysis and visualization of longitudinal genomic and clinical data from the AACR Project GENIE Biopharma Collaborative in cBioPortal. *Cancer Res.* **83**, 3861–3867 (2023).
37. Gutierrez Guarnizo, S. A. et al. Pathogenic signal peptide variants in the human genome. *NAR Genom. Bioinform.* **5**, lqad093 (2023).
38. Wijewickrama, G. T. et al. Unique membrane interaction mode of group IIF phospholipase A_2. *J. Biol. Chem.* **281**, 32741–32754 (2006).
39. Messeguer, X. et al. PROMO: detection of known transcription regulatory elements using species-tailored searches. *Bioinformatics* **18**, 333–334 (2002).

40. Chan, L. S. A. & Wells, R. A. Cross-talk between PPARs and the partners of RXR: a molecular perspective. *PPAR Res.* **2009**, 925309 (2009).
41. Arafeh, R., Shibue, T., Dempster, J. M., Hahn, W. C. & Vazquez, F. The present and future of the Cancer Dependency Map. *Nat. Rev. Cancer* **25**, 59–73 (2025).
42. Mei, S. et al. Cistrome Data Browser: a data portal for ChIP-Seq and chromatin accessibility data in human and mouse. *Nucleic Acids Res.* **45**, D658–D662 (2017).
43. Lamas Bervejillo, M. et al. A FABP4–PPARγ signaling axis regulates human monocyte responses to electrophilic fatty acid nitroalkenes. *Redox Biol.* **29**, 101376 (2019).
44. King, J. L., Smithers, L., Vrielink, A., Lesterhuis, W. J. & Piggott, M. J. A new era for PPARγ: covalent ligands and therapeutic applications. *J. Med. Chem.* **68**, 23705–23750 (2025).
45. Askari, B. et al. Rosiglitazone inhibits acyl-CoA synthetase activity and fatty acid partitioning to diacylglycerol and triacylglycerol via a peroxisome proliferator–activated receptor-γ–independent mechanism in human arterial smooth muscle cells and macrophages. *Diabetes* **56**, 1143–1152 (2007).
46. Yao-Borengasser, A. et al. Stearoyl-coenzyme A desaturase 1 gene expression increases after pioglitazone treatment and is associated with peroxisomal proliferator-activated receptor-γ responsiveness. *J. Clin. Endocrinol. Metab.* **93**, 4431–4439 (2008).
47. Li, J. et al. Targeting JMJD6/PPARγ/GPX4 axis overcomes ferroptosis resistance and enhances therapeutic efficacy in hepatocellular carcinoma. *Oncogene* **44**, 4377–4390 (2025).
48. Koch, J. et al. Unequivocal mapping of molecular ether lipid species by LC–MS/MS in plasmalogen-deficient mice. *Anal. Chem.* **92**, 11268–11276 (2020).
49. Xia, T. et al. Deep-profiling of phospholipidome via rapid orthogonal separations and isomer-resolved mass spectrometry. *Nat. Commun.* **14**, 4263 (2023).
50. Mahoney-Sanchez, L. et al. α Synuclein determines ferroptosis sensitivity in dopaminergic neurons via modulation of ether-phospholipid membrane composition. *Cell Rep.* **40**, 111231 (2022).
51. Guo, C. C. et al. Molecular profile of bladder cancer progression to clinically aggressive subtypes. *Nat. Rev. Urol.* **21**, 391–405 (2024).
52. Tate, T. et al. Pparg signaling controls bladder cancer subtype and immune exclusion. *Nat. Commun.* **12**, 6160 (2021).
53. Halstead, A. M. et al. Bladder-cancer-associated mutations in RXRA activate peroxisome proliferator-activated receptors to drive urothelial proliferation. *eLife* **6**, e30862 (2017).
54. Eray, A. & Özhan, S. Classification of bladder cancer cell lines according to regulon activity. *Turk J. Biol.* **45**, 656–666 (2021).
55. Cheng, X., Wang, Y., Li, Y. & Liu, W. Quantification of ferroptosis pattern in bladder carcinoma and its significance on immunotherapy. *Sci. Rep.* **12**, 9066 (2022).
56. Liu, J. et al. Ferroptosis mediation patterns reveal novel tool to implicate immunotherapy and multi-omics characteristics in bladder cancer. *Front. Cell Dev. Biol.* **10**, 791630 (2022).
57. Vicidomini, C. et al. An aging-sensitive compensatory secretory phospholipase that confers neuroprotection and cognitive resilience. Preprint at *bioRxiv* https://doi.org/10.1101/2024.07.26.605338 (2024).
58. da Silva, T. F., Sousa, V. F., Malheiro, A. R. & Brites, P. The importance of ether-phospholipids: a view from the perspective of mouse models. *Biochim. Biophys. Acta* **1822**, 1501–1508 (2012).
59. Mortensen, M. S., Ruiz, J. & Watts, J. L. Polyunsaturated fatty acids drive lipid peroxidation during ferroptosis. *Cells* **12**, 804 (2023).
60. Dennis, E. A., Cao, J., Hsu, Y. H., Magrioti, V. & Kokotos, G. Phospholipase A_2 enzymes: physical structure, biological function, disease implication, chemical inhibition, and therapeutic intervention. *Chem. Rev.* **111**, 6130–6185 (2011).
61. Kim, D. H. et al. Farnesoid X receptor protects against cisplatin-induced acute kidney injury by regulating the transcription of ferroptosis-related genes. *Redox Biol.* **54**, 102382 (2022).
62. Tschuck, J. et al. Farnesoid X receptor activation by bile acids suppresses lipid peroxidation and ferroptosis. *Nat. Commun.* **14**, 6908 (2023).
63. Bi, G. et al. Retinol saturase mediates retinoid metabolism to impair a ferroptosis defense system in cancer cells. *Cancer Res.* **83**, 2387–2404 (2023).
64. Tschuck, J. et al. Suppression of ferroptosis by vitamin A or radical-trapping antioxidants is essential for neuronal development. *Nat. Commun.* **15**, 7611 (2024).
65. Tonnus, W. et al. Multiple oestradiol functions inhibit ferroptosis and acute kidney injury. *Nature* **645**, 1011–1019 (2025).

Methods

Chemicals

IKE (S8877), fenofibrate (S1794) and bexarotene (S2098) were purchased from Selleck Chemicals. (1*S*,3*R*)-RSL3 (Cayman Chemicals 19288), liproxstatin 1 (Cayman Chemicals 17730), PE-18:0/20:4 (1-stearoyl-2-arachidonoyl-*sn*-glycerol-3-PE; Cayman Chemicals 25871), PE-18:0/18:1 (1-stearoyl-2-oleoyl-*sn*-glycero-3-PE; Cayman Chemicals 38153) and PC-18:0/20:4 (1-stearoyl-2-arachidonyl-*sn*-glycero-3-PC; Cayman Chemicals 10009864) were purchased from Cayman Chemicals. GW1929 (MedChemExpress HY-15655) and rosiglitazone (MedChemExpress HY-17386) were purchased from MedChemExpress. PE-P-18:0/20:4 (C18(Plasm)-20:4 PE, Avanti 852804) was purchased from Avanti Research.

Cell culture

HT1080 cells, HEK293T cells and their derived cell lines were cultured in DMEM (provided by the Media Preparation Core Facility of the Memorial Sloan Kettering Cancer Center (MSKCC)) with 10% fetal bovine serum (Gibco), 2 mM L-glutamine and 100 U ml^{-1} penicillin/streptomycin (Gibco) at 37 °C and 5% CO_2. RT112, SW780, RT4 and T47D cells and their derived cell lines were cultured in RPMI (provided by the Media Preparation Core Facility of MSKCC) with 10% fetal bovine serum (Gibco), 2 mM L-glutamine and 100 U ml^{-1} penicillin/streptomycin (Gibco) at 37 °C and 5% CO_2. 253 J, T24 and HT1376 cells were cultured in Eagle's MEM (provided by the Media Preparation Core Facility of MSKCC) with 10% fetal bovine serum (Gibco), 2 mM L-glutamine and 100 U ml^{-1} penicillin/streptomycin (Gibco) at 37 °C and 5% CO_2.

The HT1080 (CCL-121), HEK293T (CRL-3216), SW780 (CRL-2169), RT4 (HTB-2), T24, HT1376 (HTB-4) and T47D (HTB-133) cell lines were acquired through ATCC. The RT112 and 253 J cell lines were a gift from the laboratory of David Solit. T47D MBOAT1^{KO} cells were obtained as described[5]. Batch-specific certificates of analysis are available on the manufacturer's website from ATCC. The RT112 and 253 J cell lines were not authenticated.

Cell lines

Generation of PLA2G2F overexpression cell lines. Different constructs for *PLA2G2F* cDNAs were subcloned into the pQCXIP vector with a Flag-tag at the C-terminus. The plasmids were confirmed using Sanger sequencing. To generate stable overexpression, retroviral particles of the corresponding plasmids were made as shown in the Production of lentiviral and retroviral infectious particles. HT1080 and RT112 cells were infected with retroviruses and selected with 2 μg ml^{-1} puromycin.

Generation of PLA2G2F-H110Q cells. The PLA2G2F-H110Q plasmid was made from the isoform 2 overexpression plasmid using the Q5 Site-Directed Mutagenesis Kit (NEB, E0554s) with the following primers: PLA2G2F_H110Q_F (CTGCCACGCCCAGGACTGCTGCT) and PLA2G2F_H110Q_R (CACCAGTCCACCTCATCCTTGGG) for H110Q. The mutation was confirmed using Sanger sequencing. To generate stable overexpression, retroviruses of the corresponding plasmids were made as shown in the Production of lentiviral and retroviral infectious particles. RT112 cells were infected with retroviruses and selected with 2 μg ml^{-1} puromycin.

Generation of PLA2G2F ΔL53–V57 and A61Y/G63Y cells. The PLA2G2F ΔL53–V57 and A61Y/G63Y plasmids were made from the isoform 2 overexpression plasmid using the following primers and amplified with KAPA HiFi HotStart ReadyMix (Roche, KK2601): dL53-V57_F (CTGTCCACAGCTCACG) and dL53-V57_R (GTGAGCTGTGGACAGGATGGCCACG) for ΔL53–V57 and A61Y_G63Y_F (TCCACATATCACTACAGCCTGCTCAAC) and A61Y_G63Y_R (TGCCGTGAGCTGTGGACAGAACGCTGC) for A61Y/G63Y. The linear PCR product was circularized with In-Fusion Snap Assembly Master Mix (Takeda, 638949) and confirmed with Sanger sequencing. To generate stable overexpression, retroviruses of the corresponding plasmids were made as shown in the Production of lentiviral and retroviral infectious particles. RT112 cells were infected with retroviruses and selected with 2 μg ml^{-1} puromycin.

Generation of PLA2G2F CRISPR knockout cells. RT112-PLA2G-2F^{KO} cells were generated by transient transfection of two *PLA2G2F* targeting sgRNAs (GGTCAGTGGAACCATAACTC and GAGATGGAATCCTCCAGGGA) cloned in the eSpCas9(1.1)-T2A-eGFP or eSpCas9(1.1)-T2A-mCherry vector, respectively (Addgene, 71814), in RT112 cells with Lipofectamine 3000 reagent (Invitrogen, L3000001). The cells were sorted for GFP$^+$mCherry$^+$ cells by FACS 48–72 h after transfection and plated for single clones. Single clones were selected by genomic PCR confirming the deletion of *PLA2G2F* exon 2 using primers PLA2G2F_KO_F (AACATGGCAGATGGGGCAAAGGCCA) and PLA2G2F_KO_R (ATGATGCCGGGACGAGTGGCAGGGT).

Generation of cells overexpressing signal peptide–GFP fusion protein. The signal peptide–GFP fusion cDNAs were cloned from the eGFP coding sequence and were amplified from a template plasmid using the following primers: SP_eGFP_F (GTCCACAGCTCACGGCgtgagcaagggcgag) and eGFP_XhoI_R (ATCGTATGGGTACATCTCGAGTCCGctacttgtacagctcgtcca). The N-terminal signal peptide of PLA2G2F was then appended to the eGFP sequence through successive rounds of overlapping PCR extension. In each round, the forward primer was extended upstream using overlapping primers (TGGCCATCCTTGCTGGCAGCGTTCTGTCCACAGCTCAC, GTGCCACCATGAAGAAGTTCTTCACCGTGGCCATCCTTGCTGG and GGAATTGATCCGCGGCCGCACCGGTGCCACCATGAAGA subsequently) to complete the full-length signal peptide sequence. The final PCR product was subcloned into a linearized pQCXIP retroviral vector digested with AgeI and XhoI, and the plasmid was verified by Sanger sequencing. To generate stable overexpression, retroviruses of the corresponding plasmids were made as shown in the Production of lentiviral and retroviral infectious particles. RT112 cells were infected with retroviruses and selected with 2 μg ml^{-1} puromycin.

Generation of endogenous HA-tagged PLA2G2F. PLA2G2F_dTAG_HA_Neo plasmid was generated by subcloning the two homology arms in FKBP-V(dTAG)_2xHA_P2A_Neo[66]. The two homology arms were generated using genomic PCR in RT112 wild-type cells with the following primers: overhang1_F (TCGCCTTCTTGACGAGTTCTTCTAGAGCCTCTGAGGTTTGAGAGA) and overhang1_R (ATGATTACGCCAAGCTTGATGCCTGGGGGGTGTACCTGGGTGTGT) and overhang2_F (TAAAACGACGGCCAGTGAATTCGATGGGTGACTTAGGTAAACCCA) and overhang2_R (ACCAGAACCACCACCAGAACCACCGGGAGGGGCGGGGGGCGCTGG).

RT112 cells were transiently transfected with an sgRNA (GCCCCTCCCTAGAGCCTCTG) subcloned in eSpCas9(1.1)-T2A-eGFP (Addgene, 71814) and PLA2G2F_dTAG_HA_Neo with Lipofectamine 3000 and sorted by FACS for GFP-positive cells. Sorted cells were then subjected to selection with 100 μg ml^{-1} genecitin G415 (Gibco, 10131035) and plated for single clones. Single clones with a homozygous HA tag insert were confirmed by genomic PCR using the primers PLA2G2F_HA_testF (ACAGCCTTTGCCACCCCATC) and PLA2G2F_HA_testR (GGCCATCCTGTGGGATCAGC) and by western blot.

Generation of PPARG KD cells. For the generation of PPARG KD cell lines, lentiviral plasmid constructs of *PPARG* shRNA (Sigma-Aldrich, TRCN0000001670 and TRCN0000001671) or its control plasmid (Sigma-Aldrich, shc001) were purchased from MilliporeSigma. To generate stable overexpression, lentiviruses of the corresponding plasmids were made as shown in the Production of lentiviral and retroviral infectious particles. RT112 cells were infected with retroviruses and selected with 2 μg ml^{-1} puromycin.

Production of lentiviral and retroviral infectious particles

Retroviruses were produced by cotransfecting the retroviral plasmid, packaging plasmid *gag/pol* (Addgene, 14887) and pCMV-VSV-G plasmid (Addgene, 8454) into HEK293T by Lipofectamine 3000 reagent (Invitrogen, L3000001). Lentiviruses were produced by cotransfecting lentiviral plasmid, packaging plasmid psPAX2 (Addgene, 12260) and pMD2.G plasmid (Addgene, 12259) into HEK293T cells by coprecipitation with calcium phosphate. The supernatants containing infectious particles were collected 48 h after transfection and passed through a 0.45-μm filter.

Immunoblotting

Cells were harvested and lysed in RIPA buffer (Thermo Fisher Scientific, 89900) with protease inhibitor (Thermo Fisher Scientific A32955). Cell debris was removed by centrifuging at 12,000 *g* for 10 min, and the supernatant was collected. Protein concentrations were determined by Protein Assay Dye Reagent Concentrate (Bio-Rad 5000006). 4× Laemmli buffer was added to the cell lysate with appropriate concentration, and the samples were subjected to boiling at 95 °C for 5 min. Cell lysates were then resolved on SDS–PAGE gels and transferred to a nitrocellulose membrane. The membranes were blocked in 5% milk (RPI, M17200) at room temperature for 30 min and then incubated with primary antibodies at 4 °C overnight. After three washes in TBST, the membranes were incubated with goat anti-mouse horseradish peroxidase (HRP)-conjugated antibody (Invitrogen, 31430) or goat anti-rabbit HRP-conjugated antibody (Invitrogen, 31460) at room temperature for 30 min and then subjected to three washes in TBST. The membranes were then incubated for 5 min for chemiluminescence in Clarity Western ECL Substrate (Bio-Rad, 1705060) and visualized by Amersham Imager 600 (GE Healthcare Life Sciences).

The following primary antibodies were used: vinculin antibody (7F9) (Santa Cruz Biotechnology, sc-73614), 1:1,000; monoclonal anti-Flag M2 antibody (Sigma-Aldrich, F1804), 1:1,000; HA-tag (C29F4) rabbit monoclonal antibody (Cell Signaling Technology, 3724S), 1:1,000; FABP4 (E6E8B) rabbit monoclonal antibody (Cell Signaling Technology, 50699 T), 1:1,000; ACSL4 antibody (F-4) (Santa Cruz Biotechnology, sc-365230), 1:100; and PPARγ (C26H12) rabbit monoclonal antibody (Cell Signaling Technology, 2435S), 1:1,000.

qRT–PCR

Cells were lysed using TRIzol solution (Invitrogen, 15596026) after the indicated treatments. Total RNA was extracted following the manufacturer's instructions. cDNAs were synthesized using iScript Reverse Transcription Supermix (Bio-Rad, 1708841), and qPCR was performed using PowerUp SYBR Green Master Mix (Applied Biosystems, A25742). *GADPH* was used as the internal control. The relative expression of the indicated genes was calculated by the $\Delta\Delta C_T$ method. A list of the primers used for qPCR is provided in Supplementary Table 2.

Collection and concentration of the conditioned medium

Cells were cultured at an appropriate density for at least 24 h. Conditioned medium was collected and concentrated to one-tenth of its original volume using an Amicon Ultra Centrifugal Filter, 10 kDa MWCO (UFC8010) at 3,200 *g* for 30 min.

PNGase F assay

To remove N-linked oligosaccharides on PLA2G2F, 20 μg of lysate and the corresponding volume of concentrated conditioned medium were adjusted subsequently for the following buffer: 0.25% SDS, 50 mM dithiothreitol, preheated at 95 °C for 5 min, 50 mM Tris-HCl (pH 7.5) and 1% NP-40. 6U PNGase F (6 U; Promega, V4831) was added to the reaction mix, and the reaction was incubated at 37 °C for 3 hr. 4× Laemmli buffer was added to the treated samples and was ready to be resolved by SDS–PAGE gels.

Cell death assay

Cells were seeded at an appropriate cell density and cultured under normal conditions for 24 h. Cells were then stained with 0.1 μg ml^{-1} Hoechst 33342 (Invitrogen, H3570) for 20 min at 37 °C followed by treatments as described in individual experiments with 5 nM SYTOX Green to monitor cell death. Culture plates were read by Cytation 5 at the indicated time points. The percentage of cell death was calculated as the number of SYTOX $Green^+$ cells divided by the number of Hoechst 33342^+ cells. Cystine starvation media were made using the corresponding media for each cell line deprived of cyst(e)ine (provided by the Media Preparation Core Facility of MSKCC) with 10% dialyzed fetal bovine serum (GeminiBio, 100-108-500), 2 mM L-glutamine and 100 U ml^{-1} penicillin/streptomycin (Gibco).

Cell viability assay

Cells were seeded at an appropriate cell density in a 96-well plate and cultured under normal conditions for 24 h. Cells were then treated with the indicated treatments as described in individual experiments in 100 μl medium per well. Fifty microliters of CellTiter-Glo reagent (Promega, G7573) was added to each well, and the plates were shaken for 2 min and incubated at room temperature for 10 min. Fifty microliters per well of incubated reagent was transferred to an opaque white plate and measured for luminescence using a Spark Multimode Microplate Reader (Tecan).

Measurement of lipid ROS

Cells were seeded at an appropriate cell density and cultured under normal conditions in 24-well plates. Then, cells were treated with RSL3 for 3 h, followed by staining with 5 μM BODIPY 581/591 C11 (Invitrogen, D3861) for 30 min at 37 °C. The cells were then washed twice with PBS and trypsinized for flow cytometry analysis with 0.1 μg ml^{-1} DAPI (Invitrogen, D1306). Flow cytometry data were collected using the BD FACSDiva software with an LSRFortessa instrument. Initial cells were identified by gating SSC-A versus FSC-A. Single-cell events were identified by gating FSC-H versus FSC-A, and live cells were gated by DAPI-A versus FSC-A (Supplementary Fig. 3). Lipid ROS levels were quantified by measuring the mean fluorescence intensity of the oxidized C11-BODIPY signal in the FITC-A channel. All data were normalized to control groups for statistical analysis and representation in bar plots.

In vitro PLA2G2F activity assay

Sample preparation and in vitro reaction. Control, PLA2G2F isoform 2- and PLA2G2F-H110Q-overexpressing RT112 cells were harvested from 85% confluent 15-cm plates in lysing buffer (50 mM Tris-HCl (pH 8.0), 150 mM sodium chloride (NaCl), 0.5% Triton X-100 and 5% glycerol (v/v)) containing protease inhibitor (Thermo Scientific, A32955). Samples were centrifuged at 12,000 *g* for 10 min, and the supernatant was collected and measured for protein concentration using the BCA assay. Five milligrams of lysate was incubated with anti-Flag M2 affinity gel (MilliporeSigma, A2220) at 4 °C overnight. The Flag-binding gel was washed three times with reaction buffer (50 mM HEPES (pH 7.4), 100 mM NaCl and 50 μM butylated hydroxytoluene (BHT)) for the lipid reaction.

Individual 1 mM lipid stocks of PE-18:0/18:1, PE-18:0/20:4, PE-P-18:0/20:4 and PC-18:0/20:4 were prepared in chloroform. For lipid film preparation, 100 μl of each lipid stock was combined to a 200-μl total lipid volume per condition, with the following three paired lipid conditions: PE-18:0/18:1 with PE-18:0/20:4, PE-18:0/20:4 with PE-O-18:0/20:4 and PE-18:0/20:4 with PC-18:0/20:4. BHT was added to a final concentration of 50 μM. Lipids were dried under a gentle stream of nitrogen and left uncapped for 10 min to remove residual solvent. Dried lipid films were resuspended in 1 ml reaction buffer (50 mM pH 7.4 HEPES, 100 mM NaCl and 50 μM BHT), yielding a final concentration of 200 μM total lipid. Samples were vortexed briefly, incubated at room

temperature for 15 min, vortexed again and sonicated for 5 min at 4 °C. Liposome suspensions were stored at 4 °C for up to 24 hr.

Biochemical reaction and LC–MS processing. Washed Flag affinity gel and 25 µl liposome mix were combined to a total volume of 100 µl in reaction buffer, with the addition of 0.5 mM $CaCl_2$. The reaction mixture was incubated at 37 °C for 30 min, spinning at 500 rpm. EDTA was added to a final concentration of 2 mM to quench the reaction, and 100 pmol fatty acid 17:0 was added as an internal standard. Lipids were extracted by sequential addition of 300 µl ice-cold methanol and 1,000 µl methyl-tert-butyl ether (MTBE) containing 0.01% BHT, incubated at 4 °C for 2 h and phase separated by centrifugation. The upper organic layer was collected for analysis.

Chromatographic separation was performed using an ACQUITY Premier UPLC system coupled to a SYNAPT XS mass spectrometer (Waters Corporation) equipped with an ACQUITY Premier CSH C18 column (1.7 µm, 2.1×100 mm) at 65 °C. Peak areas for substrates and products were extracted using TargetLynx software (Waters Corporation), background subtracted and normalized against internal standards to compute substrate hydrolysis percentages and LPL-to-phospholipid (LPL/phospholipid) ratios. Detailed information regarding the mobile phase configurations, gradient elution tables and mass spectrometer gas/ionization parameters is provided in the Supplementary Methods.

Immunoprecipitation label-free proteomics analysis

Sample preparation. RT112 cells with PLA2G2F overexpression were harvested from two 85% confluent 10-cm plates per sample for immunoprecipitation. The samples were washed twice with ice-cold PBS and collected in 300 µl RIPA buffer (Thermo Scientific, 89900) with protease inhibitor (Thermo Scientific A32955). A BCA assay was performed to confirm the amount of protein collected in each sample, and the samples were incubated with 10 µl of anti-Flag M2 beads (Sigma, A2220) per 1 mg lysate at 4 °C overnight. Captured protein complexes were washed three times with ice-cold RIPA, three times with ice-cold PBS and once with ddH_2O. The pull-down fraction was then incubated with 100 µl of 1% SDS at 55 °C and 1,000 rpm for 5 min and eluted in a Spin-X tube, 0.45 µm pore CA membrane (Corning, 8163).

Label-free analysis was conducted on immunoprecipitated samples. Eluates (in 1% SDS) underwent disulfide bond reduction with 5 mM TCEP at room temperature for 10 min, followed by alkylation with 25 mM iodoacetamide at room temperature for 20 min. A buffer clean-up step using SP3 paramagnetic beads was performed before protease digestion[67]. Samples were resuspended in 100 mM EPPS pH 8.5 and digested at 37 °C for 6 h with 0.5 µg trypsin. Each sample was desalted via StageTip, dried again via vacuum centrifugation and reconstituted in 5% acetonitrile and 1% formic acid for liquid chromatography–tandem mass spectrometry (LC–MS/MS) processing.

Peptides were loaded onto a microcapillary column with an inner diameter of 100 µm packed in house with ~ 30 cm of HALO Peptide ES-C18 resin and separated using an UltiMate 3000 RSLCnano UHPLC system connected to an Orbitrap Eclipse Tribrid mass spectrometer equipped with a FAIMS Pro Interface (Thermo Scientific). The complete LC solvent gradients and detailed FAIMS/DDA configuration states are documented in the Supplementary Methods.

Mass spectra were processed using the FragPipe software pipeline (v22.0)[68] and the LFQ-MBR workflow. Spectra were converted to mzML using MSConvert software[69] and matched with peptide sequences with a composite sequence database including the UniProt human reference proteome, as well as sequences of common contaminants and the specific PLA2G2F sequence used for re-expression. Proteins were quantified by the IonQuant module[70] using default parameters for measurements of MaxLFQ intensities and match between runs. Protein quantification values were exported for further analysis in Microsoft Excel and FragPipe-Analyst[71]. A median-centered normalization strategy was applied, with no imputation performed. Gene Ontology analysis (cellular component) was conducted within FragPipe Analyst. Annotations for bona fide ER organellar protein markers were assembled from proteins that scored with confidence 'very high' or 'high' confidence in a previously published HeLa dataset[72]. Detailed analysis methods are provided in the Supplementary Methods.

ChIP–qPCR. Two million RT112 cells were fixed with 1% formaldehyde for 10 min at room temperature and quenched with 0.125 M glycine. Nuclei were isolated, resuspended in SDS immunoprecipitation buffer and sheared using a Covaris E220 Focused-ultrasonicator for 15 min to yield DNA fragments spanning 200–600 bp. Sheared chromatin was cleared by centrifugation at 20,000*g* for 30 min. Chromatin samples were diluted and incubated with 625 ng of anti-PPARG (Cell Signaling Technology, 2435S) or normal rabbit IgG control antibody (Cell Signaling Technology, 2729S) overnight at 4 °C, followed by captured binding to Dynabeads Protein A (Invitrogen, 10001D). Immunoprecipitated complexes were washed thoroughly through low-salt and high-salt buffers. Crosslinks were reversed by overnight incubation at 65 °C in elution buffer containing 1% SDS. Purified DNA fractions were isolated using the QIAquick PCR Purification Kit (Qiagen) and analyzed by qPCR with PowerUp SYBR Green Master Mix. Enrichment was calculated relative to the total input chromatin DNA percentage. Detailed buffer conditions and primer sequences are provided in the Supplementary Methods and Supplementary Table 3.

Immunofluorescence. Cells were seeded at an appropriate cell density and cultured under normal conditions for 24 h on a glass chamber (Nunc Lab-Tek II Chamber Slide System, Thermo Scientific, 154534PK). After 24 h, the medium was removed, and cells were fixed with 4% formaldehyde in PBS at room temperature for 10 min. Fixed cells were washed three times with ice-cold PBS and permeabilized with ice-cold methanol at −20 °C for 10 min. After washing three times with PBS, cells were blocked with BK buffer (1% BSA, 10% goat serum (Sigma-Aldrich, G9023) in PBS, passed through a 0.22-µm filter) at room temperature for 30 min and stained with primary antibody diluted in BK buffer at 4 °C overnight. Cells were then stained with secondary antibodies (goat anti-mouse IgG H&L (Alexa Fluor 647), Abcam, ab150115-1001 and goat anti-rabbit IgG H&L (Alexa Fluor 488), Abcam, ab150077-1001) at 1:1,000 in BK buffer at room temperature for 30 min, followed by staining with DAPI at 1:10,000 in PBS. The cells were washed three times with PBS and subjected to the addition of ProLong Gold Antifade Mountant with DAPI (Invitrogen, P36935) and covered with a coverslip before confocal microscopy (Leica, SP8). To quantify colocalization of PLA2G2F, cells were individually masked, and Pearson's coefficients were calculated by the Coloc2 plugin in Fiji (ImageJ) using the Flag signal and the corresponding cellular organelle signal within each mask.

The following antibodies were used: monoclonal anti-Flag M2 antibody (Sigma-Aldrich, F1804), 1:50; PDI (C81H6) rabbit monoclonal antibody (Cell Signaling Technology, 3501S), 1:100; COX IV (3E11) rabbit monoclonal antibody 4850 (Cell Signaling Technology, 4850S), 1:400; and Golgin-97 polyclonal antibody (Invitrogen, PA5-30048), 1:200.

Lipidomic analysis

Sample preparation and processing. Five biological replicates of RT112 cells (comparing PLA2G2F overexpression versus empty vector control and PLA2G2F knockout versus wild-type controls) were harvested by scraping in ice-cold PBS containing 0.001% BHT. Aliquots were reserved for protein normalization via the BCA assay, and the remaining pellets were snap frozen in liquid nitrogen.

Lipids were extracted from frozen cell pellets homogenized in 300 µl LC–MS-grade ice-cold methanol with 0.01% butylated hydroxyl toluene using a microtip sonicator. Homogenized cells were transferred to fresh glass vials with 1,000 µl ice-cold MTBE and 1 µl Avanti SPLASH LIPIDOMIX Mass Spec Standard (splashmix) and vortexed

vigorously. Samples were left to incubate overnight at −20 °C. The next day, 250 µl of LC–MS-grade water was added to the samples and left to incubate on ice for 20 min, after which they were centrifuged at 1,800 *g* for 20 min at 4 °C. Approximately 600 µl of the lipid-containing organic upper phase of MTBE was collected into new LC–MS-grade glass vials and dried down under a gentle stream of nitrogen gas. Dried samples were reconstituted in 100 µl of 2-propanol/acetonitrile/water (4:3:1, v/v/v). A quality-control sample was prepared by combining 20 µl of each sample to assess the reproducibility of the features through the LC–MS runs, as well as to gather fragmentation data using HDMSE data acquisition for lipid annotation.

LC–MS conditions and analysis. Lipids from samples were separated and analyzed using an ACQUITY UPLC system coupled to a SYNAPT XS (Waters Corporation) ion mobility time-of-flight mass spectrometer equipped with an electrospray ionization source that was used in negative ion mode[73,74]. Detailed separation and acquisition parameters are described in the Supplementary Methods.

Lipidomic LC–MS/MS data were first converted to a vendor-neutral format (.mzml) via MS Convert[69], and postprocessing was achieved using MS-DIAL (version 5.5.250627)[75,76]. Data were searched against the database (Msp20250409095351_NCDK_conventional_converted_dev.) for lipid identification with the following searching parameters: accurate mass tolerance (MS^1) set at 0.01 Da and (MS^2) set at 0.025 Da. Types of adduct ion for consideration included $[M\text{-}H]^-$ and $[M + CH_3COO]^-$. Alignment was based on retention time tolerance of 0.1 min and MS^1 tolerance of 0.015 Da. All lipid species were manually inspected with their MS/MS spectra, and the mass list and the representative MS/MS spectra for each reported class of lipid species were included in Supplementary Table S1 and Supplementary Figs. 1and 2. The representative spectra are provided to demonstrate class-specific diagnostic fragmentation patterns (for example, head group ions, neutral losses and fatty acyl fragments). For statistical analysis, MS-CleanR was enabled to filter the results with a minimum blank ratio set at 0.8 and to delete ghost peaks, incorrect mass was checked and relative standard deviation was set at a maximum of 20. Alignment results were further normalized by signal intensities of Avanti SPLASH LIPIDOMIX, and fill% was set to a minimum of 0.8.

Statistical analysis was achieved using RStudio with the packages dplyr, t.test and p.adjust for conducting multiple *t* tests to acquire adjusted *P* values (Bonferroni correction) of group comparisons. The resulting data were then graphically represented for statistical significance using GraphPad Prism 10.

Statistics and reproducibility

Please refer to the legend of the figures for a description of sample sizes and statistical tests performed. Data were plotted by GraphPad Prism 10 unless otherwise specified. Differences were considered statistically significant when the *P* value was less than 0.05 and otherwise not significant. For parametric tests, normality and equal variance were assumed but not formally tested. No statistical method was used to predetermine sample size. No data were excluded from the analyses. The investigators were not blinded to allocation during experiments and outcome assessment.

Reporting summary

Further information on research design is available in the Nature Portfolio Reporting Summary linked to this article.

Data availability

The LC–MS/MS proteomics and lipidomics raw data and supplementary files have been deposited to the ProteomeXchange Consortium via the MassIVE partner repository with the accession number MSV000098651 and shared to the PRIDE partner repository with the dataset identifier PXD066621. Source data are provided with this paper.

Code availability

Code was used in this study on RStudio to calculate the adjusted *P* values for the lipidomics dataset. The source code and accompanying dataset are provided as Supplementary Code.

References

66. Wang, H. et al. H3K4me3 regulates RNA polymerase II promoter-proximal pause-release. *Nature* **615**, 339–348 (2023).
67. Hughes, C. S. et al. Ultrasensitive proteome analysis using paramagnetic bead technology. *Mol. Syst. Biol.* **10**, 757 (2014).
68. Kong, A. T., Leprevost, F. V., Avtonomov, D. M., Mellacheruvu, D. & Nesvizhskii, A. I. MSFragger: ultrafast and comprehensive peptide identification in mass spectrometry-based proteomics. *Nat. Methods* **14**, 513–520 (2017).
69. Chambers, M. C. et al. A cross-platform toolkit for mass spectrometry and proteomics. *Nat. Biotechnol.* **30**, 918–920 (2012).
70. Yu, F., Haynes, S. E. & Nesvizhskii, A. I. IonQuant enables accurate and sensitive label-free quantification with FDR-controlled match-between-runs. *Mol. Cell Proteomics* **20**, 100077 (2021).
71. Hsiao, Y. et al. Analysis and visualization of quantitative proteomics data using FragPipe-Analyst. *J. Proteome Res.* **23**, 4303–4315 (2024).
72. Itzhak, D. N., Tyanova, S., Cox, J. & Borner, G. H. Global, quantitative and dynamic mapping of protein subcellular localization. *eLife* **5**, e16950 (2016).
73. Lu, G., Xu, S., Huang, P. & Li, L. Enhancing lipidomics with high-resolution ion mobility-mass spectrometry. *Proteomics* **26**, 7–22 (2026).
74. Huang, P., Zhang, H., Liu, Y. & Li, L. Rapid characterization of phospholipids from biological matrix enabled by indium tin oxide (ITO) coated slide assisted enrichment MALDI mass spectrometry. *Anal. Sens.* **4**, e202300097 (2024).
75. Tsugawa, H. et al. MS-DIAL: data-independent MS/MS deconvolution for comprehensive metabolome analysis. *Nat. Methods* **12**, 523–526 (2015).
76. Takeda, H. et al. MS-DIAL 5 multimodal mass spectrometry data mining unveils lipidome complexities. *Nat. Commun.* **15**, 9903 (2024).
77. Jumper, J. et al. Highly accurate protein structure prediction with AlphaFold. *Nature* **596**, 583–589 (2021).
78. Mirdita, M. et al. ColabFold: making protein folding accessible to all. *Nat. Methods* **19**, 679–682 (2022).

Acknowledgements

We thank the MSKCC Flow Cytometry Core Facility for assistance with flow cytometry, and we also thank the MSKCC Molecular Cytometry Core and Z. Bian for assistance with confocal microscopy. We thank D. Solit at MSKCC for providing crucial cell lines. We also thank members of the Jiang laboratory for critical reading and suggestions. Some results for cancer patients shown here are based on data generated by the TCGA Research Network (https://www.cancer.gov/tcga) and the GTEx Portal (https://www.gtexportal.org/home/).

Author contributions

Conceptualization: Y.H., D.L. and X.J.; cellular and biochemical experiments: Y.H. and N.C.; proteomics and data analysis: A.O.; lipidomics acquisition: J.C. and P.R.; lipidomics data analysis: Y.H., P.R. and P.H.; funding acquisition: W.G., A.O., B.R.S. and X.J.; and writing: Y.H. and X.J.

Funding

This research is supported by NIH P01CA291697 (to X.J., B.S. and W.G.); NIH R01CA204232, NIH R01CA258622 and a grant from Mr. William H. and Mrs. Alice Goodwin and the Commonwealth Foundation for

Cancer Research and The Center for Experimental Therapeutics of MSKCC (to X.J.); NIH P01CA291694, R35CA253059 and R01CA258390 (to W.G.); NIH R35GM156454 (to A.O.); and NCI Cancer Center Core Grant P30 CA008748 to MSKCC.

Competing interests

X.J. and D.L. are inventors on patents related to autophagy and cell death. X.J. holds equity in and consults for Lime Therapeutics. B.R.S. is an inventor on patents and patent applications involving ferroptosis, holds equity in and serves as a consultant to ProJenX and serves as a consultant to Weatherwax Biotechnologies and Akin Gump Strauss Hauer & Feld LLP. The other authors declare no competing interests.

Additional information

Extended data is available for this paper at https://doi.org/10.1038/s41594-026-01830-7.

Supplementary information The online version contains supplementary material available at https://doi.org/10.1038/s41594-026-01830-7.

Correspondence and requests for materials should be addressed to Xuejun Jiang.

Peer review information *Nature Structural & Molecular Biology* thanks Bo Chu, Eun-Woo Lee and the other, anonymous, reviewer(s) for their contribution to the peer review of this work. Peer reviewer reports are available. Primary Handling Editors: Katarzyna Ciazynska and Carolina Perdigoto, in collaboration with the *Nature Structural & Molecular Biology* team.

https://doi.org/10.1038/s41594-026-01830-7

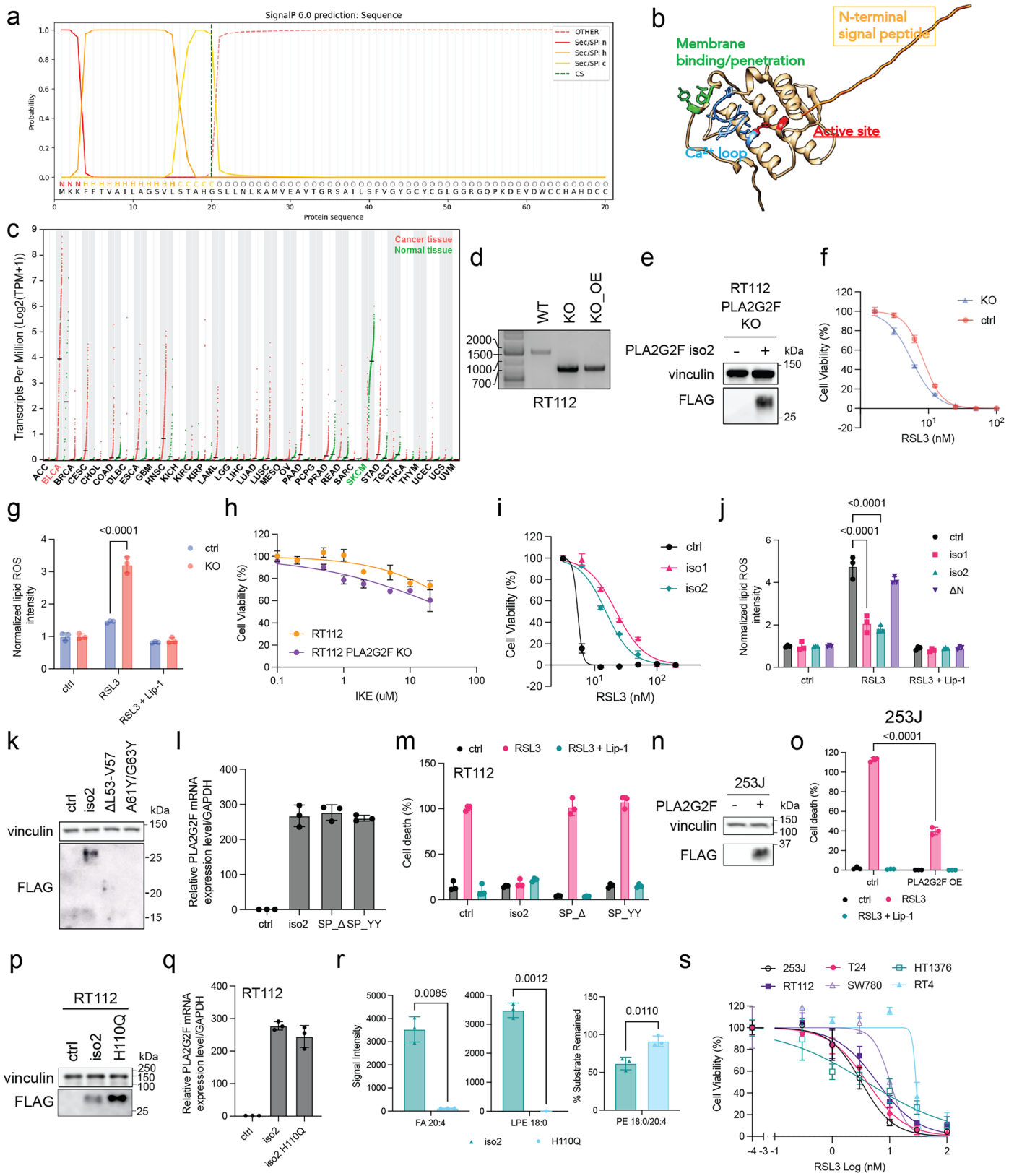

Extended Data Fig. 1 | See next page for caption.

https://doi.org/10.1038/s41594-026-01830-7

Extended Data Fig. 1 | PLA2G2F inhibits ferroptosis. a, Signal peptide is predicted at the N-terminus of PLA2G2F Isoform-1 by SignalP 6.0[14]. **b**, AlphaFold 3[77,78]-predicted structure of PLA2G2F Isoform-1.**c**, PLA2G2F expression across different cancer and normal tissues[31–33]. **d**, Confirmation of PLA2G2F knockout in RT112 cells by genomic PCR. **e**, Overexpression of PLA2G2F Isoform-2 in RT112 cells with endogenous PLA2G2F knocked out. **f**, Cell viability in control (ctrl) and PLA2G2F-KO RT112 cells, under 12.5 nM RSL3 treatment for 6 hr. **g**, Normalized lipid ROS intensity at 4 hr following 12.5 nM RSL3 treatment. **h**, RT112 cells are resistant towards IKE at 24 hr. **i**, Cell viability in RT112 ctrl cells and PLA2G2F OE cells under RSL3 treatment at 24 hr. **j**, Normalized lipid ROS intensity following 12.5 nM RSL3 treatment for 4 hr in control and PLA2G2F-overexpressing RT112 cells. **k,l**, Overexpression of indicated signal peptide mutant forms of PLA2G2F, detected by Western blot (**k**) or RT-qPCR (**l**). **m**, Signal peptide mutations show no protection towards 12.5 nM RSL3 for 20 hr. **n**, Overexpression of PLA2G2F in 253 J cell confirmed with Western blot. **o**, PLA2G2F-overexpressing 253 J cells were more resistant to ferroptosis induced by 12.5 nM RSL3 for 24 hr. **p,q**, Active site mutation overexpression detected by Western blot (**p**) or RT-qPCR (**q**). **r**, H110Q mutation shows no activity in in vitro enzymatic activity assay. **s**, Cell viability towards different RSL3 concentration across the bladder cancer panel. Cells were treated by RSL3 for 24 hr. Lip-1 (liproxstatin-1), 5 μM. Data are presented as mean ± s.d., n = 3 (**f-j, l-m, o, q-s**) biologically independent samples. Statistical analysis was performed using two-way ANOVA (**g,j,o**) or unpaired two-tailed t-test (**r**).

https://doi.org/10.1038/s41594-026-01830-7

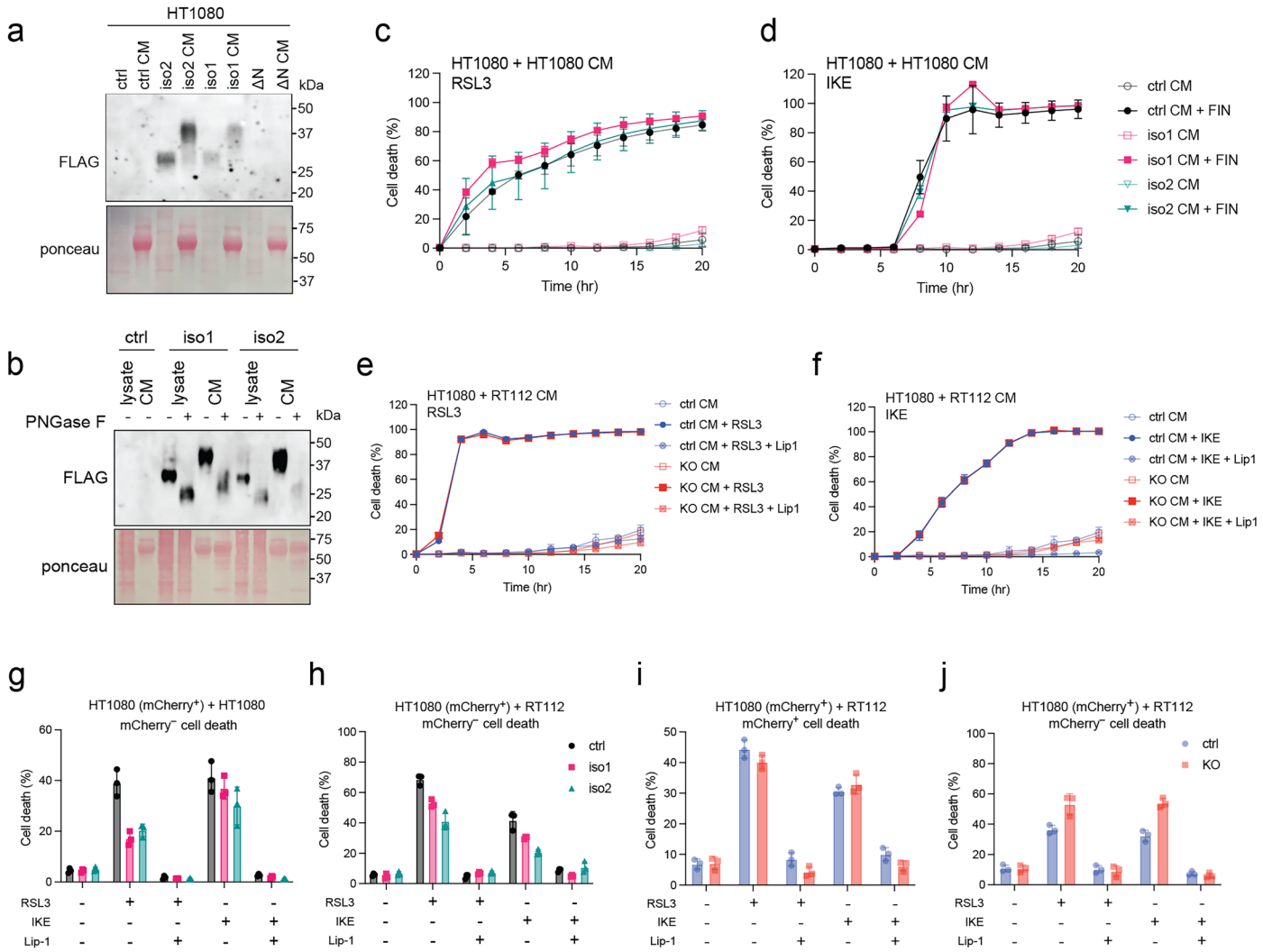

Extended Data Fig. 2 | PLA2G2F inhibits ferroptosis through intracellular mechanisms. a, Western blot of CM of PLA2G2F-overexpressing HT1080 cells. **b**, Western blot of CM or lysate of PLA2G2F-overexpressing RT112 cells, with or without treatment with PNGase F as indicated. **c,d**, Cell death curve of WT HT1080 cells cultured in CM from PLA2G2F-overexpressing HT1080 cells. Cells were treated with 25 nM RSL3 (**c**) or 0.5 μM IKE (**d**). **e,f**, Cell death curve of WT HT1080 cells cultured in CM from PLA2G2F-knockout RT112 cells. Cells were treated with 25 nM RSL3 (**e**) or 0.5 μM IKE (**f**), and/or 5 μM Lip-1 as indicated. **g,h**, mCherry$^-$ cell death in the co-culture of mCherry-H2B-labeled HT1080 cells with PLA2G2F-overexpressing HT1080 (**g**) or RT112 (**h**) cells at 12 hr. Cells were treated with 25 nM RSL3, 0.5 μM IKE, and/or Lip-1 5 μM. **i,j**, mCherry$^+$ (**i**) and mCherry$^-$ (**j**) cell death of co-cultured mCherry-H2B labeled HT1080 cells with PLA2G2F-knockout RT112 cells at 10 hr. Cells were treated with 25 nM RSL3, 0.5 μM IKE, and/or 5 μM Lip-1. Data are presented as mean ± s.d., n = 3 (**c-j**) biologically independent samples.

https://doi.org/10.1038/s41594-026-01830-7

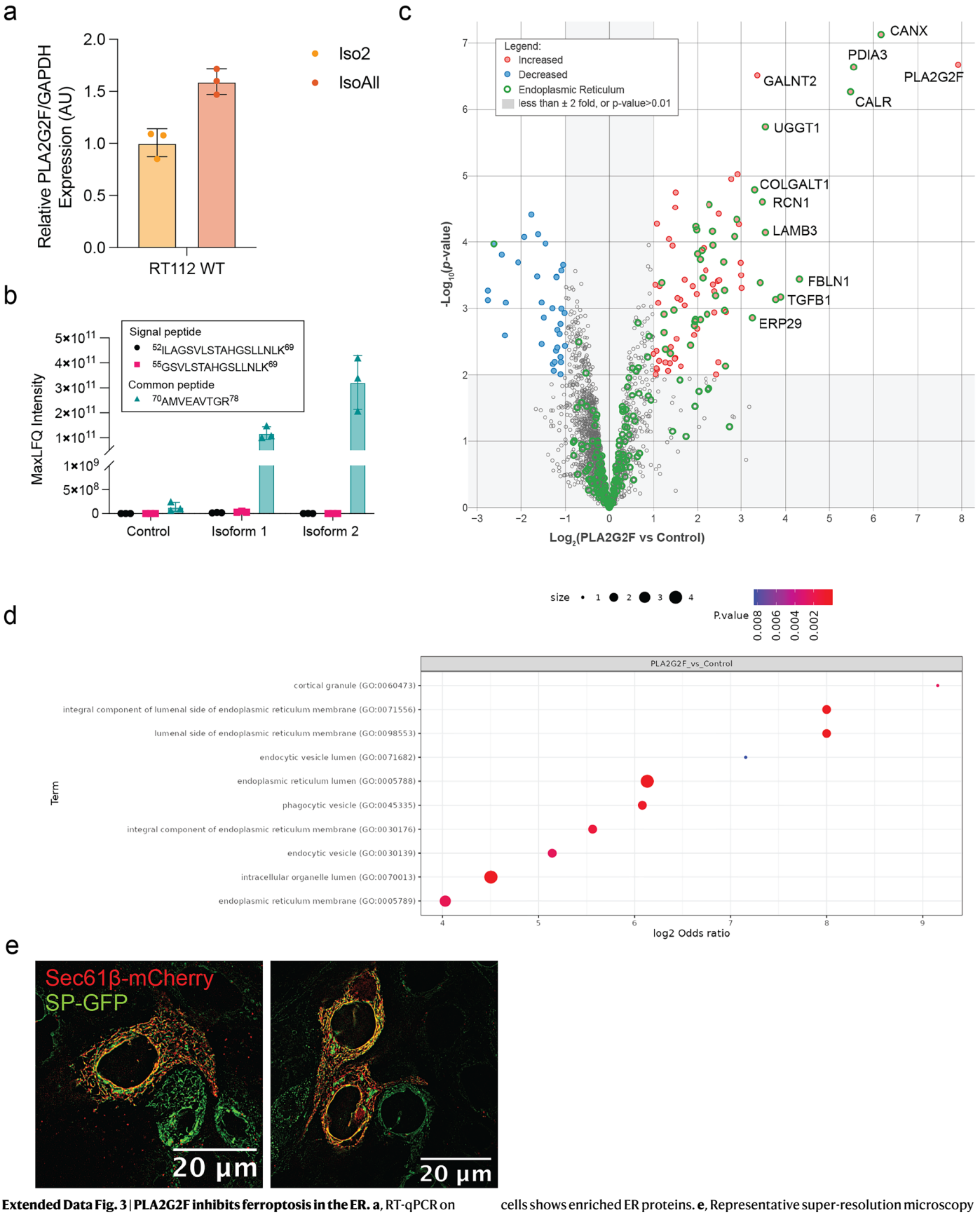

Extended Data Fig. 3 | PLA2G2F inhibits ferroptosis in the ER. a, RT-qPCR on Isoform-2-specific or signal peptide-specific mRNA sequences in WT RT112 cells. **b**, MS signal intensity of signal peptide-specific peptides and common peptides on FLAG-IP from PLA2G2F-overexpressing RT112 cells. **c**, Co-IP/MS of PLA2G2F-overexpressing RT112 cells shows enriched ER proteins. **d**, Gene Ontology (cellular component) analysis of Co-IP/MS of PLA2G2F-overexpressing RT112 cells shows enriched ER proteins. **e**, Representative super-resolution microscopy showed colocalization of GFP fused with the PLA2G2F signal peptide with ER membrane marker Sec61β-mCherry from n = 2 independent experiments. Data are presented as mean ± s.d., n = 3 (**a**-**b**) biologically independent samples. Statistical analysis was performed using unpaired two-tailed t-test with adjusted p-value (Benjamini-Hochberg correction) (**c**).

https://doi.org/10.1038/s41594-026-01830-7

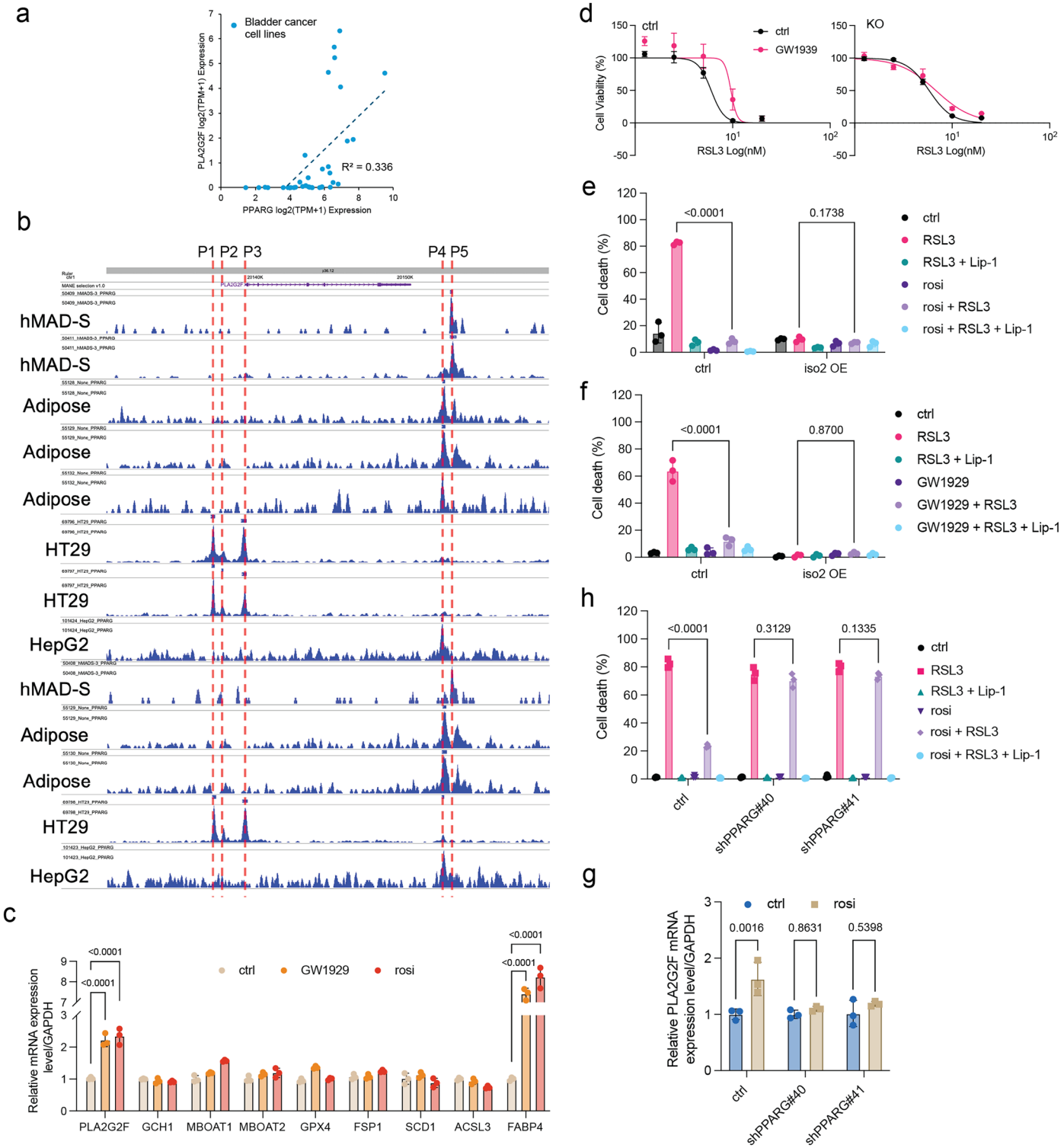

Extended Data Fig. 4 | PPARG suppresses ferroptosis in a PLA2G2F-mediated manner in bladder cancer cells. a, Positive correlation of PPARG expression with PLA2G2F expression in bladder cancer cell lines. **b**, ChIP databases of PPARG binding to PLA2G2F, varying between different cell lines. **c**, Effect of PPARG agonist on ferroptosis-related genes (48-hr agonist treatment). **d**, Cell viability of control and PLA2G2F-KO RT112 cells after RSL3 treatment for 24 hr (48-hr agonist treatment). **e,f**, Cell death of RT112 cells with PLA2G2F-isoform 2 overexpressed. Cells were pretreated with rosiglitazone (**e**) or GW1929 (**f**) for 48 hr and then subjected to RSL3 for 24 hr. **g**, RT-qPCR of PPARG-knockdown RT112 cells treated with rosiglitazone for 48 hr. **h**, Cell death of RT112 cells with PPARG knockdown and with 20 μM rosiglitazone (48 hr pretreatment) at 14 hr. GW1929, 10 μM; rosiglitazone (rosi), 20 μM; RSL3, 12.5 nM; Lip-1 (liproxstatin-1), 5 μM. Data are presented as mean ± SD, n = 3 (**c**-**h**) biologically independent samples. Statistical analysis was performed using two-way ANOVA (**c**-**f**,**h**) or unpaired two-tailed t-test (**g**).

https://doi.org/10.1038/s41594-026-01830-7

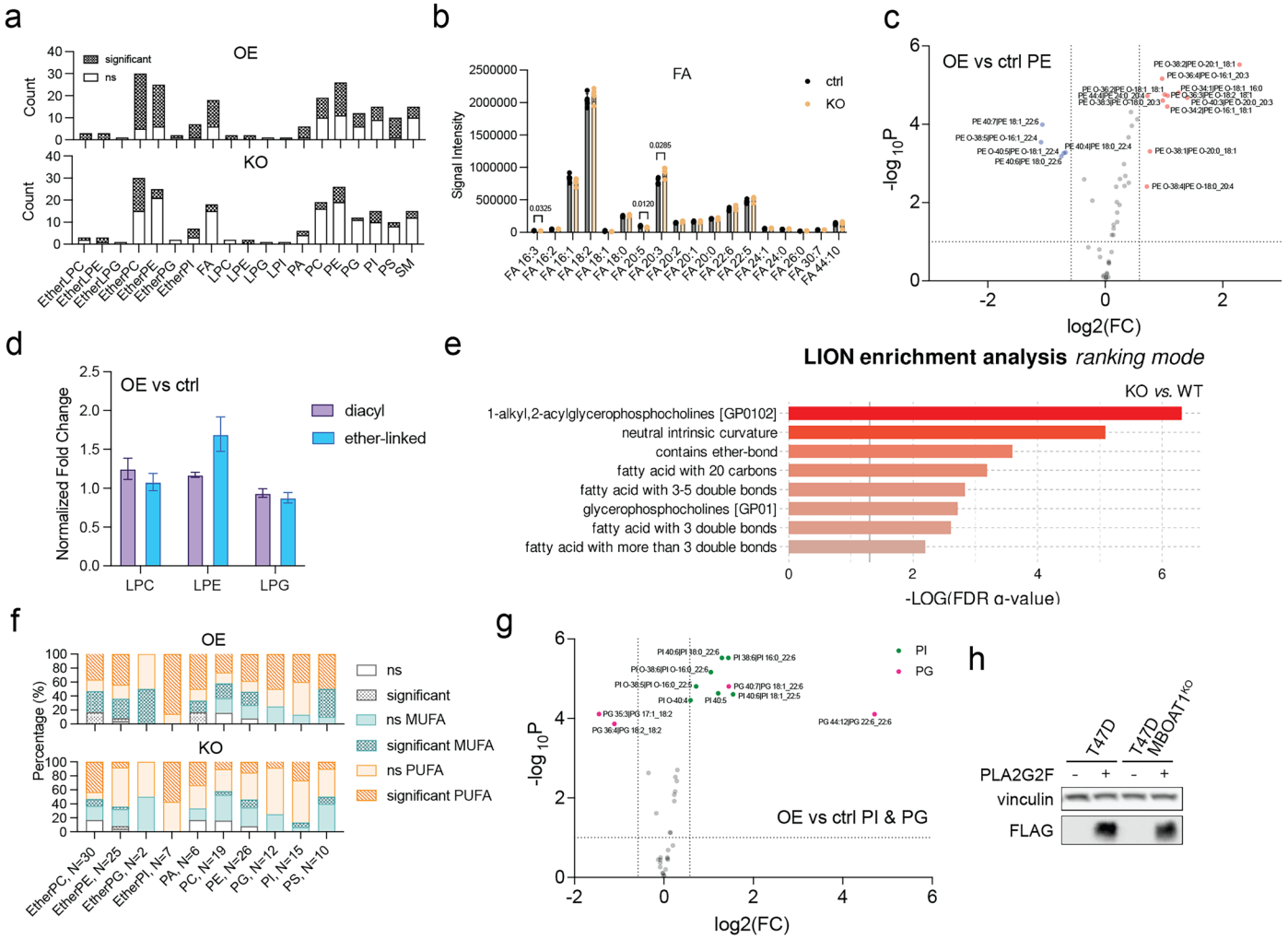

Extended Data Fig. 5 | Lipidomic analysis of the effect of PLA2G2F on cellular lipidome. a, Number of lipids identified and quantified as statistically significant according to their lipid species in PLA2G2F OE vs ctrl RT112 cells (upper panel) and KO vs WT RT112 cells (lower panel). **b**, Lipidomic intensity of identified FAs in PLA2G2F KO vs ctrl cells. **c**, Volcano plot of lipidomic analysis PLA2G2F OE vs control RT112 cells, showing PE and ether PE species. **d**, Normalized LPL fold change from the lipidomic analysis of PLA2G2F OE vs control group. **e**, Top hits of LION enrichment analysis of lipidomic analysis of PLA2G2F KO vs WT cells. **f**, Percentage of significant PLs with MUFA or PUFA tails among each lipid species in PLA2G2F OE vs ctrl RT112 cells (upper panel) and KO vs WT RT112 cells (lower panel). **g**, Volcano plot of lipidomic analysis PLA2G2F OE vs control RT112 cells, showing PI and ether PI species (green), and PG and ether PG species (magenta). **h**, Western blot showing PLA2G2F overexpression in control or MBOAT1-KO T47D cells from n = 2 independent experiments. Data are presented as mean ± SD, n = 5 (**b**) biologically independent samples or median ± SE_{Median} (**d**) calculated as the median abundance of detected lysophospholipid species divided by the median abundance of corresponding phospholipid species for each condition. Statistical analysis was performed using unpaired two-tailed t-test with adjusted p-value (Bonferroni correction) (**c**,**g**). Note that due to the isobaric nature of plasmanyl (O-) and plasmenyl (P-) species, ether-linked lipids are annotated based on MS-DIAL output; however, theses assignments remain structurally ambiguous at the MS1 and MS2 levels.

nature portfolio

Corresponding author(s): Xuejun Jiang

Last updated by author(s): May 24, 2026

Reporting Summary

Nature Portfolio wishes to improve the reproducibility of the work that we publish. This form provides structure for consistency and transparency in reporting. For further information on Nature Portfolio policies, see our Editorial Policies and the Editorial Policy Checklist.

Statistics

For all statistical analyses, confirm that the following items are present in the figure legend, table legend, main text, or Methods section.

n/a	Confirmed
☐	☒ The exact sample size (*n*) for each experimental group/condition, given as a discrete number and unit of measurement
☐	☒ A statement on whether measurements were taken from distinct samples or whether the same sample was measured repeatedly
☐	☒ The statistical test(s) used AND whether they are one- or two-sided *Only common tests should be described solely by name; describe more complex techniques in the Methods section.*
☒	☐ A description of all covariates tested
☐	☒ A description of any assumptions or corrections, such as tests of normality and adjustment for multiple comparisons
☐	☒ A full description of the statistical parameters including central tendency (e.g. means) or other basic estimates (e.g. regression coefficient) AND variation (e.g. standard deviation) or associated estimates of uncertainty (e.g. confidence intervals)
☐	☒ For null hypothesis testing, the test statistic (e.g. *F*, *t*, *r*) with confidence intervals, effect sizes, degrees of freedom and *P* value noted *Give P values as exact values whenever suitable.*
☒	☐ For Bayesian analysis, information on the choice of priors and Markov chain Monte Carlo settings
☒	☐ For hierarchical and complex designs, identification of the appropriate level for tests and full reporting of outcomes
☐	☒ Estimates of effect sizes (e.g. Cohen's *d*, Pearson's *r*), indicating how they were calculated

Our web collection on statistics for biologists contains articles on many of the points above.

Software and code

Policy information about availability of computer code

Data collection	Confocal microscopy data were collected by Leica Application Suite X. Cell death data were collected by BioSPA. IP-MS were collected on Orbitrap Eclipse Tribrid mass spectrometer (Thermo Fisher Scientific). Lipidomics data were collected using Synapt-XS (Waters Corp.).
Data analysis	FragPipe software pipeline, MSConvert, MS-DIAL, R Studio, R, Prism, ImageJ (Fiji), Microsoft Excel, Gen 5

For manuscripts utilizing custom algorithms or software that are central to the research but not yet described in published literature, software must be made available to editors and reviewers. We strongly encourage code deposition in a community repository (e.g. GitHub). See the Nature Portfolio guidelines for submitting code & software for further information.

Data

Policy information about availability of data

All manuscripts must include a data availability statement. This statement should provide the following information, where applicable:

- Accession codes, unique identifiers, or web links for publicly available datasets
- A description of any restrictions on data availability
- For clinical datasets or third party data, please ensure that the statement adheres to our policy

All data generated or analyzed during this study are included or provided in the manuscript or supplementary information files.

Research involving human participants, their data, or biological material

Policy information about studies with human participants or human data. See also policy information about sex, gender (identity/presentation), and sexual orientation and race, ethnicity and racism.

Reporting on sex and gender	This study does not involve human participants or use human data.
Reporting on race, ethnicity, or other socially relevant groupings	This study does not involve human participants or use human data.
Population characteristics	This study does not involve human participants or use human data.
Recruitment	This study does not involve human participants or use human data.
Ethics oversight	This study does not involve human participants or use human data.

Note that full information on the approval of the study protocol must also be provided in the manuscript.

Field-specific reporting

Please select the one below that is the best fit for your research. If you are not sure, read the appropriate sections before making your selection.

☒ Life sciences ☐ Behavioural & social sciences ☐ Ecological, evolutionary & environmental sciences

For a reference copy of the document with all sections, see nature.com/documents/nr-reporting-summary-flat.pdf

Life sciences study design

All studies must disclose on these points even when the disclosure is negative.

Sample size	No statistical calculations were performed to predetermine sample size.
Data exclusions	No data were excluded from the analysis.
Replication	All experiments presented in this study yielded reproducible results for a minimum of 2-3 independent replicates.
Randomization	Samples were allocated into experimental groups based on predefined genotypes, treatments, or transgene expression status, depending on the specific experiment. As this study primarily used established cell lines and engineered isogenic cell models under controlled in vitro conditions, formal randomization was not implemented.
Blinding	Investigator blinding was not performed because all experimental readout relied on objective quantitative measurements. Samples from different experimental groups were processed in parallel under identical experimental conditions, minimizing potential investigator bias during data acquisition and analysis.

Reporting for specific materials, systems and methods

We require information from authors about some types of materials, experimental systems and methods used in many studies. Here, indicate whether each material, system or method listed is relevant to your study. If you are not sure if a list item applies to your research, read the appropriate section before selecting a response.

Materials & experimental systems

n/a	Involved in the study
☐	☒ Antibodies
☐	☒ Eukaryotic cell lines
☒	☐ Palaeontology and archaeology
☒	☐ Animals and other organisms
☒	☐ Clinical data
☒	☐ Dual use research of concern
☒	☐ Plants

Methods

n/a	Involved in the study
☒	☐ ChIP-seq
☐	☒ Flow cytometry
☒	☐ MRI-based neuroimaging

Antibodies

Antibodies used	Western blots: Vinculin Antibody (7F9) (Santa Cruz sc-73614), 1:1000; Monoclonal ANTI-FLAG® M2 antibody (Sigma F1804), 1:1000;

Antibodies used	HA-Tag (C29F4) Rabbit mAb (Cell Signaling Technology 3724S), 1:1000; FABP4 (E6E8B) Rabbit mAb (Cell Signaling Technology 50699T), 1:1000; ACSL4 Antibody (F-4) (Santa Cruz sc-365230), 1:100; PPARγ (C26H12) Rabbit mAb (Cell Signaling Technology 2435S), 1:1000. ChIP qPCR: PPARγ (C26H12) Rabbit mAb, Cell Signaling Technology 2435S and Normal Rabbit IgG, Cell Signaling Technology 2729S
Validation	Antibodies were only used for applications and organisms verified by the manufacturer.

Eukaryotic cell lines

Policy information about cell lines and Sex and Gender in Research

Cell line source(s)	HT1080 (CCL-121), HEK293T (CRL-3216), SW780 (CRL-2169), RT4 (HTB-2), T24, HT1376 (HTB-4), and T47D (HTB-133) cell lines were acquired through ATCC. RT112 and 253J cell lines were a gift from the David Solit lab.
Authentication	Batch specific certificates of analysis are available at the manufacturer's website from ATCC. RT112 and 253J cell lines were not certificated.
Mycoplasma contamination	Cell lines were tested negative for mycoplasma contamination.
Commonly misidentified lines (See ICLAC register)	None.

Plants

Seed stocks	*Report on the source of all seed stocks or other plant material used. If applicable, state the seed stock centre and catalogue number. If plant specimens were collected from the field, describe the collection location, date and sampling procedures.*
Novel plant genotypes	*Describe the methods by which all novel plant genotypes were produced. This includes those generated by transgenic approaches, gene editing, chemical/radiation-based mutagenesis and hybridization. For transgenic lines, describe the transformation method, the number of independent lines analyzed and the generation upon which experiments were performed. For gene-edited lines, describe the editor used, the endogenous sequence targeted for editing, the targeting guide RNA sequence (if applicable) and how the editor was applied.*
Authentication	*Describe any authentication procedures for each seed stock used or novel genotype generated. Describe any experiments used to assess the effect of a mutation and, where applicable, how potential secondary effects (e.g. second site T-DNA insertions, mosiacism, off-target gene editing) were examined.*

Flow Cytometry

Plots

Confirm that:

☒ The axis labels state the marker and fluorochrome used (e.g. CD4-FITC).

☒ The axis scales are clearly visible. Include numbers along axes only for bottom left plot of group (a 'group' is an analysis of identical markers).

☒ All plots are contour plots with outliers or pseudocolor plots.

☒ A numerical value for number of cells or percentage (with statistics) is provided.

Methodology

Sample preparation	Cells were seeded at an appropriate cell density and cultured in normal condition in 24-well plates. Then, cells were than treated with RSL3 for 3 hours, followed by staining of BODIPY™ 581/591 C11 (Invitrogen™ D3861) 5 μM for 30 min at 37□C. The cells were then washed twice with PBS and trypsinized for flow cytometry analysis with 0.1 μg/mL DAPI (Invitrogen™ D1306).
Instrument	LSRFortessa
Software	Data were collected using BD FACSDiva software and analyzed using FlowJo and R.
Cell population abundance	Ranging from 40 to 70%.
Gating strategy	Initial cells were identified by gating SSC-A vs. FSC-A. Single-cell event were identified by gating FSC-H vs. FSC-A, and live cells were gated by DAPI-A vs. FSC-A.

☒ Tick this box to confirm that a figure exemplifying the gating strategy is provided in the Supplementary Information.